2010

Data Fusion for the Problem of Protein Sidechain Assignment

Yang Lei
University of Massachusetts Amherst

DATA FUSION FOR THE PROBLEM OF PROTEIN SIDECHAIN ASSIGNMENT

A Thesis Presented

by

YANG LEI

Submitted to the Graduate School of the
University of Massachusetts Amherst in partial fulfillment
of the requirements for the degree of

MASTER OF SCIENCE IN ELECTRICAL AND COMPUTER ENGINEERING

September 2010

Electrical and Computer Engineering

DATA FUSION FOR THE PROBLEM OF PROTEIN SIDECHAIN ASSIGNMENT

A Thesis Presented

by

YANG LEI

Approved as to style and content by:

Ramgopal R. Mettu, Chair

Paul Siqueira, Member

Dennis L. Goeckel, Member

C. V. Hollot, Department Head
Electrical and Computer Engineering

To my great parents and grandparents...

ACKNOWLEDGMENTS

I am very grateful for my advisor Prof. Ramgopal Mettu's instructions and help. He always encourages me and inspires me with lots of valuable insights in our meetings. He is an easy-going professor and also a very helpful friend to me. After I get fascinated by the area of Microwave Remote Sensing, he generously supports my thoughts and approves me to select whatever courses I like. We also aim to make the types of the techniques described in the thesis applicable in both bioinformatics and remote sensing. There is an old Chinese phrase saying "He who teaches me for one day is my father for life". I will always remember Prof. Mettu's help and this fantastic two-year master study. I would like to thank Prof. Paul Siqueira and Prof. Dennis Goeckel very much for their constructive suggestions and the favor of being my committee members. Finally, I want to give my genuine thanks to my great parents and grandparents without whom I cannot be who I am now.

ABSTRACT

DATA FUSION FOR THE PROBLEM OF PROTEIN SIDECHAIN ASSIGNMENT

SEPTEMBER 2010

YANG LEI

M.S., UNIVERSITY OF MASSACHUSETTS AMHERST

Directed by: Professor Ramgopal R. Mettu

In this thesis, we study the problem of protein side chain assignment (SCA) given multiple sources of experimental and modeling data. In particular, the mechanism of X-ray crystallography (X-ray) is re-examined using *Fourier analysis*, and a novel probabilistic model of X-ray is proposed for SCA's decision making. The relationship between the measurements in X-ray and the desired structure is reformulated in terms of *Discrete Fourier Transform* (DFT). The decision making is performed by developing a new resolution-dependent electron density map (EDM) model and applying *Maximum Likelihood* (ML) estimation, which simply reduces to the *Least Squares* (LS) solution. Calculation of the confidence probability associated with this decision making is also given. One possible extension of this novel model is the real-space refinement when the continuous conformational space is used.

Furthermore, we present a data fusion scheme combining multi-sources of data to solve SCA problem. The merit of our framework is the capability of exploiting multi-sources of information to make decisions in a probabilistic perspective based on *Bayesian inference*. Although our approach aims at SCA problem, it can be easily transplanted to solving for the entire protein structure.

TABLE OF CONTENTS

LIST OF TABLES

Table **Page**

LIST OF FIGURES

Figure **Page**

CHAPTER 1

INTRODUCTION

It is known that studying protein 3D structures is of great importance to understand the biological processes at a molecular level. Since there is a close relationship between protein structures and functionalities, we can exploit 3D structures for biomedical purposes, e.g. developing new drugs. There are currently more than 60,000 protein structures deposited in Protein Data Bank (PDB). As the experimental methods become more high-throughput, researchers are seeking efficient computational methods to assist in interpreting data for protein structure determination. Currently, the most effective experimental method for 3D structure determination is X-ray crystallography, although other techniques complement it providing additional useful information.

A typical protein 3D structure is comprised of a backbone (i.e. main chain) and side chains, where the backbone mainly describes the protein folding characteristics and side chains are detailed structure. At a high level, for a protein under test, we usually get the primary sequence according to the transcription and translation from DNA segments, and utilize experimental data to resolve potential variations of the backbone and the side chains respectively. In most existing softwares (e.g. O, XtalView), there are several standard criteria to obtain the backbone carbon atom positions [31]. By searching a database of refined backbone fragments, the main chain can finally be resolved with high accuracy.

The determination of side chain conformations, also known as *side chain assignment* (SCA), is a different and challenging problem since the measurements of side

chains are usually much poorer than those for the main chain. In this thesis, we only focus on the SCA problem; however, solving the entire protein structure is our ultimate goal, and we expect that our method can be extended to also handle backbone tracing. Current state-of-the-art methods attacking the SCA problem can be divided into two categories. The first class of methods predict side chain conformations with the principle of global minimum energy, since it is always assumed the native protein structure is a stable and dynamic equilibrium among all the possible conformations, hence minimizing the total potential energy. However, results for this type of methods are not accurate due to our limited understanding of the protein folding mechanism and the expression of the protein potential energy. The second class of methods seek to determine protein structures experimentally. In fact, each of the deposited protein structures in PDB was either solved by X-ray crystallography (X-ray) or Nuclear Magnetic Resonance (NMR). The data interpretation of both X-ray and NMR has already been studied with a wealth of valuable results brought forward. For X-ray, the process of data interpretation is usually carried out in reciprocal- and real-space refinements. This is especially in reciprocal space, since there is a shortage of effective models for real space. However, the improved experimental techniques, e.g. Multi-wavelength Anomalous Diffraction (MAD), have recently renewed the general interest in real-space refinement, which is more suited to fitting partial model to X-ray data. In this thesis, we derive a novel framework of real-space refinement based on Fourier analysis.

Researchers have also attempted to combine the experimental methods with stereochemical restraints (i.e. derived from the potential energy) to overcome overfitting the structural model to the data. The potential energy calculations, also known as stereochemical restraints, through sophisticated techniques, manage to explain many types of molecular force fields and thus eliminate the undesirable conformations. It is also noticed that each data source has some limitations regarding predicting the

protein structure accurately. Trials are made to combine different sources of data but few systematic ways are brought forward. The type of this hybrid model is commonly referred to as *Data Fusion*. Here we apply a fusion scheme for protein side chain assignment (SCA) problem using Bayesian estimation theory.

1.1 Protein Structure

Since there is a close relationship between functionality and structure, in this section, we introduce the geometric conventions for representing protein structure.

1.1.1 Amino Acid and Backbone

A protein is a compound that consists of chains of amino acids (See Fig. 1.1(a)); there are twenty types of common amino acids. Each type of amino acid shares a carbon atom (denoted by C_α), which is attached to an amine group and a carboxylic acid group. Types of amino acids differ in the *side chain* (denoted as R in Fig. 1.1(a)). Multiple amino acids undergo the condensation reaction eliminating water molecules, and forming a sequence of amino acid residues and peptides.

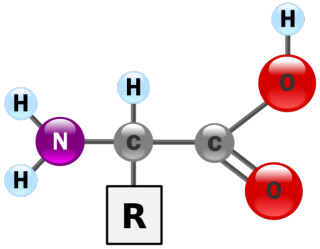

(a) Amino Acid

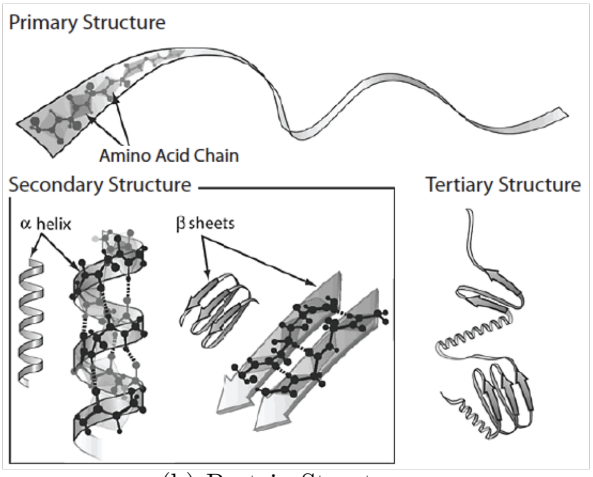

(b) Protein Structure

Figure 1.1. Amino Acid and Protein Structure. The chemical composition of an amino acid [36]. The primary, secondary and tertiary structure of a protein [3].

As a result, the polypeptide chain in (Fig. 1.1(b)) is called the protein primary structure. To differentiate from side chains, we refer to the sequence comprised of C_α atoms and peptides as the *backbone*. Furthermore, we refer to the α-helix and β-sheet as the secondary structure, and the three dimensional coordinates of all the atoms as the tertiary structure.

1.1.2 Dihedral Angles

Since the peptide forms a stable plane structure, which is much more rigid than any other bonds, the freedom of the protein folding is mostly based on the torsion angles in the backbone and the side chain. This is illustrated in Fig. 1.2. As shown, dihedral angles ϕ and ψ denote the torsion angles of the backbone peptide, and χ_1, χ_2, χ_3, χ_4 are the dihedral angles within the side chain. Note the χ angles are assigned hierarchically meaning some side chains may not have all the four χ angles.

1.1.3 Side Chain and Rotamers

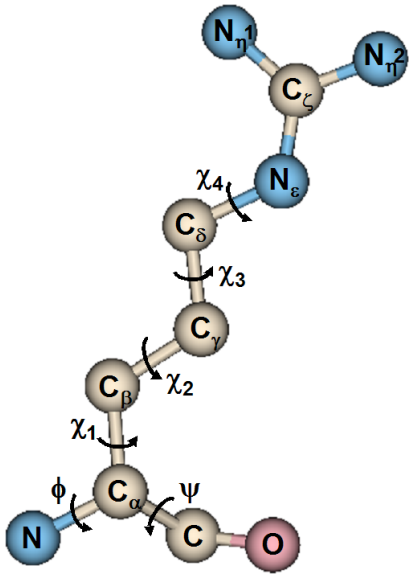

Figure 1.2. Dihedral Angles [21].

In Section 1.1.2, we noted that the side chain conformations can be represented by the possible combinations of the χ angles. Since there are four dihedral-angle degrees of freedom, there can be infinitely many combinations of $(\chi_1, \chi_2, \chi_3, \chi_4)$. Each combination of the side chain dihedral angles define a unique side chain conformation, usually denominated as a *rotational isomer* or *rotamer* [12] as shown in Fig. 1.3. Technically, researchers find out that only a finite subset of rotamers are observed for each residue type [12].

Also, it is known that not all the rotamers occur with equal frequency (e.g. there is some frequency distribution over the rotamers of each particular residue type). The most widely used rotamer libraries [11][24] are thus constructed storing the frequency information of each rotamer for certain residue type. These rotamer libraries fall into two categories, backbone-dependent libraries and backbone-independent ones. They only differ in whether to use the information of the ϕ and ψ backbone dihedral angles. Obviously, the backbone-dependent rotamer libraries are more useful and informative. In the work described here, the *Dunbrak Backbone-Dependent Rotamer Library* [11] was chosen.

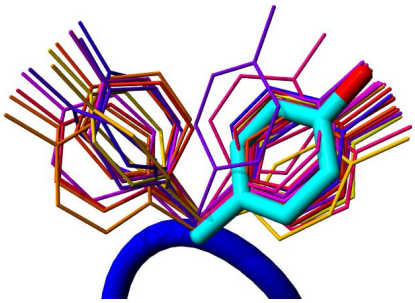

Figure 1.3. Rotamers [42].

1.2 Definition of Electron Density Map

To interpret and model X-ray data, also known as *Electron Density Map* (EDM), we need to describe the electron cloud. The most accurate description of electron cloud is given by quantum mechanics; however, due to the complexity of calculation, we prefer the classical view of electron density model. Above all, it is necessary to have an overview about the form of the electron cloud.

It was reported in September 2009 that, physicists photographed the carbon electron cloud Fig. 1.4 for the very first time.

In quantum mechanics, an electron does not exist as a single point, but spreads around a nuclei as cloud referred to as orbital. In Fig. 1.4, there are two arrangements of electron cloud for a carbon atom. As an extension of this, other atoms, such as oxygen, nitrogen and sulfur, have their own corresponding electron clouds as well. The intensity of a bright blue point in Fig. 1.4 represents the sum of the probabilities that each of the electrons is present at this current point, which can be computed by the well-known *Schrödinger* equation with lots of effort. The calculation is computa-

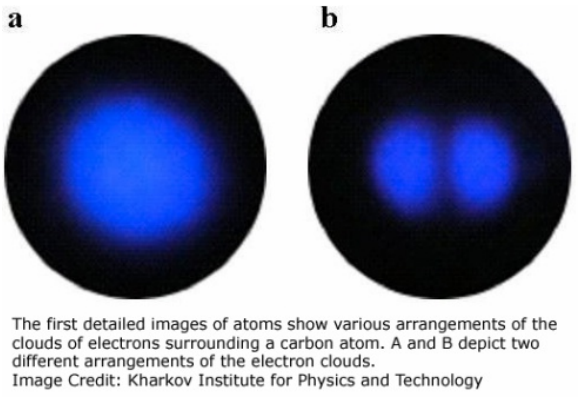

Figure 1.4. Carbon Atomic Electron Cloud [25].

tionally intractable when the electron clouds pertaining to a covalent bond should be addressed, which is rather common in protein structures. For the above mentioned reasons, we need to develop a simplified electron cloud model, which will be discussed in Section 2.2. In this section, we give a definition of electron number density and electron (number) density map.

Definition 1 (Electron Number Density and Electron Density Map)**.** Electron number density $\rho(\vec{r})$ at a point $\vec{r} = (x, y, z)$, by meaning, is the number of electrons enclosed by a closed surface as the volume approaches zero. When the position vector $\vec{r}$ goes over a single unit cell of the crystal, the three dimensional electron density function $\rho(\vec{r})$ is the widely-used *Electron Density Map (EDM).*

Definition 1 is equivalent to the above mentioned probability-based definition in quantum mechanics. Moreover, this is the ideal case meaning no resolution limitation is involved. As we will see later (Section 2.3), the effect of resolution makes the practical electron density value deviate from the ideal value $\rho(\vec{r})$, and the EDM is thus blurred. Generally, the higher the resolution is, the closer the electron density value is to $\rho(\vec{r})$, and thus the higher quality of EDM.

1.3 Definition of Protein SCA Problem

Now we define our problem of side chain assignment as follows.

Definition 2 (Side Chain Assignment)**.** The side chain conformation at a particular residue i ($1 \leq i \leq N$) is determined by selecting the most likely rotamer from the rotamer set Θ_i given that residue's backbone atoms and ϕ, ψ dihedral angles if using the backbone-dependent library. The criterion of selection in terms of likelihood could be the EDM fit, NMR restraints and stereochemical restraints, etc.

If a protein has N residues as a whole, the set of the side chain conformational space is a Cartesian product $\Theta_1 \times \Theta_2 \times \cdots \times \Theta_N$, denoted by Θ. Let $\underline{S}$ represent a candidate side chain conformation for all N residues of the current protein, and we can rewrite the above mentioned problem in a mathematical way.

$$\begin{aligned} \underline{S}^* &= \arg\max_{\underline{S}\in\Theta} P(\underline{S} \mid EDM, NMR) \\ &= \arg\max_{\underline{S}\in\Theta} f(EDM, NMR \mid \underline{S})\ P(\underline{S}) \end{aligned} \tag{1.1}$$

Given the structure, different sources of experimental data are assumed to be class-conditionally independent [38].

$$\begin{aligned} \underline{S}^* &= \arg\max_{\underline{S}\in\Theta} f(EDM, NMR \mid \underline{S})\ P(\underline{S}) \\ &= \arg\max_{\underline{S}\in\Theta} f(EDM \mid \underline{S})\ f(NMR \mid \underline{S})\ P(\underline{S}) \end{aligned} \tag{1.2}$$

In (1.2), $P(EDM \mid \underline{S})$ comes from the likelihood of X-ray data. Given the structure, the electron densities of different voxels in the crystal can be made independent (see Chapter 3). In other words, $P(EDM \mid \underline{S})$ can be broken down to individual terms $P(LEDM \mid S_i)$ associated with local electron density map (LEDM), where S_i represents the side chain conformation of the ith residue. Similarly, $P(NMR \mid \underline{S})$ can be expanded to pairwise terms in the form of $P(LNMR \mid S_i \ and \ S_j)$ after the decorrelation of NMR data. As for the priors $P(\underline{S})$, we can use Boltzmann relationship [16][41] accounting for the contribution of the potential energy function, which is comprised with self- and pairwise- energy terms.

1.4 Related Work

1.4.1 Real-space Refinement

The idea of real-space refinement is first introduced by Diamond [8], where a Gaussian electron cloud model is demonstrated. Although this refinement is successful for several proteins with high-quality EDM's, the modeled EDM does not take the resolution limitation into account. Also, since before multiple isomorphous replacement and multi-wavelength anomalous dispersion are used to give phase measurements, only amplitudes of structure factors can be measured, it is necessary to estimate the phase information using molecular replacement [31]. The EDM's constructed utilizing this inaccurate phase information are definitely not reliable for real-space fitting. However, only amplitudes of structure factors are needed for reciprocal-space refinement, which surpasses real-space refinement from then on. For the definitions of reciprocal- and real-space refinements, we draw an analogy between X-ray crystallography and Signal Processing (SP). Since structure factors and electron densities are continuous Fourier series pair, we can consider real space as time domain in SP, and reciprocal space as frequency domain. Through reciprocal-space refinement, only the amplitude information of measured structure factors is refined; however, as for real-space refinement, the electron densities, or equivalently the complex structure factors, are improved, since they are a continuous Fourier series pair.

Maximum Likelihood (ML) is a well-known technique for fitting the model to measurements using statistical fundamentals. To perform ML estimation, we have to find both the modeled data (i.e. *forward model*) and the fitting criterion (i.e. *error model*). Specifically, for real-space refinement, the modeled data refers to a resolution-dependent EDM model, and the fitting criterion is the probability distribution of each sampled electron density in the observed EDM, given the modeled EDM. The model of resolution-dependent EDM is given by Chapman [4], which is valid for the situation that the measurements in X-ray are truncated by a limiting sphere. For the fitting

criterion, we need to compare the modeled EDM with the EDM constructed from measurements in some reasonable way. It is necessary to mention that we could make local comparisons in real-space refinement, which does not hold for reciprocal space. The local EDM comparison can be used in reciprocal-space refinement [20] as a matching score, but the real application in real-space refinement is by Zou et al. [45]. The simple Gaussian model in [8] is used and two types of fitting measures are proposed (i.e. convolution product and absolute difference). Both measures are taken over the voxel of a amino acid in the EDM, or local EDM. However, neither of these is based on the probability distribution of the electron densities in the local EDM. We will show the error distribution of electron densities at each sampled 3D grid point in the entire EDM, which has not been looked into before. To our knowledge, the only description of real-space fitting error is the mean square error (MSE) of the entire EDM, which is derived from Parseval's Theorem [31], but not for individual sampled points.

1.4.2 Discrete Fourier Summation in Reciprocal-space Refinement

Although electron density values and structure factors are conventionally related by *Continuous Fourier Series* (CFS), it is desirable to connect them through *Discrete Fourier Summation* (DFS), which is also called *Discrete Fourier Transform* (DFT). Both reciprocal- and real-space refinements utilize the relationship between structure factors and electron densities, so the DFT representation can be used for both cases. As seen later, we can use the DFT representation for real-space refinement to achieve the probability distribution of sampled electron densities, i.e. the error model.

The DFT representations for both reciprocal- and real-space refinements turn out to be the same, but the problems of aliasing are different, since there is no truncation of structure factors (e.g. limiting sphere) in reciprocal-space refinement. So for reciprocal-space refinement, the error from aliasing can only be reduced but not

eliminated; while for real-space refinement, we can absolutely overcome the aliasing by selecting the sampling frequency appropriately.

In reciprocal-space refinement, structure factors are usually calculated by performing the DFT since it can be implemented efficiently using the *Fast Fourier Transform* (FFT). Sayre [35] first showed that the calculation of structure factors can be done using DFS, despite the fact that FFT had not been developed yet; he also discussed the problem of aliasing. Ten Eyck [39] and Navaza [28] extend Sayre's work and address the aliasing problem.

1.4.3 General Data Fusion Techniques

In classification problem using remote sensing data, Swain represents the conditional probability of each class given multi-source data by assuming different types of data are independent, and assigning the reliability weights to individual marginal probabilities [38][1]. A final decision can be made by maximizing this weighted joint likelihood. This process is usually called *pre-detection fusion*. Bennedikson and Swain [1] also show that this statistical fusion scheme is equivalent to a neural network approach. However, sometimes it is difficult to transmit the information of conditional probability due to channel limitations, researchers intend to make decisions at each local data source/sensor quantizing the observations to discrete decisions. Based on the individual local decisions, we end up with a final decision at the fusion center. Chen et al. [5] talked about the binary and M-ary *decision fusion* by performing Bayesian sampling of the posterior probability. Both schemes are carefully introduced in [19]. As for the current SCA problem, there is no issue of channel limitation involved, thus we propose to use pre-detection fusion based on Bayesian inference.

1.4.4 Data Fusion in Protein Structure Refinement

Our goal is to combine different sources of experimental data to firstly solve the SCA problem and then to determine the entire structure. The simplest fusion scheme

is a linear combination of sources of data, which can be X-ray and potential energy [2]. For X-ray, either reciprocal-space [37][15] or real-space [4] matching score is used as a pseudo-energy term along with the potential energy terms, i.e. stereochemical restraints. In these works, the linear coefficients are typically adjusted by trial and error. We will show in Chapter 5 that, our proposed fusion scheme is equivalent to this linear representation by taking the logarithm and converting probability to energy; however, our choice of parameters is on a probabilistic basis using Bayesian inference.

1.4.5 Protein Model-building Softwares using Real-space Refinement

Although most of the existing softwares for protein model-building are associated with reciprocal-space refinement, there are indeed some packages that successfully use real-space refinement.

Coot [13] uses the atomic number weighted sum of electron density values around atomic centers as an X-ray matching score, and the stereochemical restraints as a potential energy score. ARP/wARP [26] [27] merges model-building and structure refinement as a single iterative process. Specifically, a hybrid model (comprised of free-atoms and modeled atoms) and reciprocal-space refinement for building the main chain (i.e. backbone) go back and forth to improve the solution. For the side chains, ARP/wARP represents the density as a function of torsion angles and then perform a real-space torsion angle refinement. The idea of torsion angle refinement dates back to 1971, when Diamond [8] first introduced real-space refinement. The advantage of torsion-angle refinement, compared to all-atom Cartesian coordinates refinement, is the reduction of the dimension of the conformation space, or equivalently increasing the *observation to parameter ratio*. Examination of stereochemical restraints follows each iteration. Both RESOLVE [40] and TEXTAL [17] construct databases respectively comprised with accurately resolved structures and their EDM's or atomic

thermal factors. They only have X-ray matching scores, which is by comparison, between the local EDM of the unknown structure and the local EDM of some set of structure templates. As for the local EDM of the template, they either search the corresponding EDM's deposited in the database, or build a local EDM, using the atomic thermal factors stored along with the structure files. In other words, for the modeled data, neither actually calculates the local EDM from a universal model; their performances completely rely on the statistics of the database. ACMI [9] also constructs a database of structure fragments/templates but the local modeled EDM is computed for the chosen template using some techniques described vaguely in [7]. However, the idea of accounting for the resolution limitation in the modeled EDM is the same as Chapman's work [4]. ACMI also includes the stereochemical restraints as global constraints to eliminate undesirable conformations.

1.5 Outline

In Chapter 2, we explain basic background knowledge about X-ray data collection, and introduce a novel resolution-dependent EDM model. In Chapter 3, we derive and analyze a new probabilistic model for X-ray crystallographic data interpretation. We will show decision making and confidence probability calculation based on this model. In Chapter 4, we illustrate and discuss the prediction results along with confidence probabilities at varying resolutions. At last, Chapter 5 validates other possible data sources, and presents the data fusion scheme with the improved prediction results.

CHAPTER 2

X-RAY DATA COLLECTION AND RESOLUTION-DEPENDENT ELECTRON DENSITY MODEL

In Chapter 2, we introduce the background knowledge for X-ray crystallography based on Fourier analysis. In Section 2.1, we show the diffraction principle, the reciprocal space for describing the diffraction pattern, and the Fourier relationship between the electron density function and structure factors. In Section 2.2, a simple Gaussian-distributed atomic electron density model is presented. The EDM constructed from this model is called the ideal-case EDM model. By considering the effect of the resolution limitation as a filter, Section 2.3 gives a resolution-dependent EDM model, which is by meaning, a function of resolution.

2.1 X-ray Diffraction and Structure Factor

The diagram of an X-ray crystallography experiment is shown in Fig. 2.1. First, crystallographers grow a protein crystal, the conditions of which are under strict control. Then, the crystal is mounted appropriately, allowing rotation around the center. When the crystal is exposed to an intense X-ray beam, the diffraction pattern on a sensor screen as the crystal is rotated, is recorded.

When the incident wavefronts impinge on the crystal planes, since electrons of atoms are secondary radiating sources, and also the wavelength of X-ray (1-100 Å) and the spacing d between unit cells are similar in size, the superposition of scattered waves will produce a diffraction pattern. The superposed wave propagates constructively

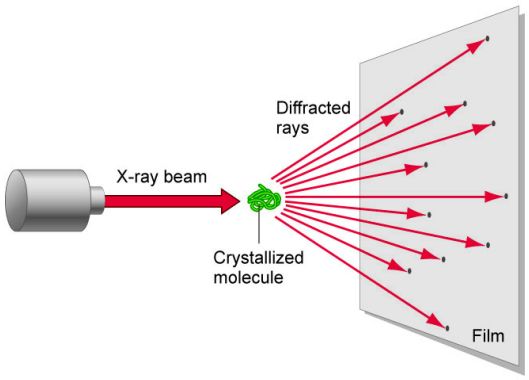

Figure 2.1. X-ray Crystallography Experiment [18].

in some directions, and destructively in others. The direction of the constructive interference is given by Bragg's equation described by

$$2d \sin\theta = n\lambda. \tag{2.1}$$

Note that the normal vector to the reflection plane bisects the angle between incident and reflected waves. As long as a set of planes are spaced equal distance apart, satisfying (2.1), we refer to these planes as imaginary reflection planes. One treatment is to increase the incident angle, θ, so that the spacing between the adjoining reflection planes can be reduced, resulting in the resolution of finer details. This is the basic idea of rotating the crystal to achieve more reflection information, which will be discussed later.

To better represent the reflections on the crystal planes, physicists use indices (h, k, l) with $(\vec{a}, \vec{b}, \vec{c})$ being the real-space basis vectors. These vectors are the edge vectors of a single unit cell in the crystal. For the reason stated below, we consider (h, k, l) as three-dimensional coordinates with respect to the reciprocal-space basis vectors $(\vec{a}^*, \vec{b}^*, \vec{c}^*)$. The relationship between $(\vec{a}, \vec{b}, \vec{c})$ and $(\vec{a}^*, \vec{b}^*, \vec{c}^*)$ is

$$\vec{a}\cdot\vec{a}^{*}=1;\vec{b}\cdot\vec{a}^{*}=0;\vec{c}\cdot\vec{a}^{*}=0$$
$$\vec{b}\cdot\vec{b}^{*}=1;\vec{a}\cdot\vec{b}^{*}=0;\vec{c}\cdot\vec{b}^{*}=0$$
$$\vec{c}\cdot\vec{c}^{*}=1;\vec{a}\cdot\vec{c}^{*}=0;\vec{b}\cdot\vec{c}^{*}=0. \tag{2.2}$$

The origin of the reciprocal space is the intersection point of the traveling direction of the incident X-ray and the Ewald sphere (as shown in Fig. 2.2), which is centered at the crystal center with a $1/\lambda$ radius (λ is the wavelength of X-ray). Crystallographers use the reciprocal-space vector $h\vec{a}^{*}+k\vec{b}^{*}+l\vec{c}^{*}$ to represent the normal vector to the reflection planes. It thus can be shown that [10], if the crystal planes with the real-space index representation (h,k,l) form a set of reflection planes, the end of the reciprocal-space vector $h\vec{a}^{*}+k\vec{b}^{*}+l\vec{c}^{*}$, or the three-dimensional reciprocal-space grid point (h,k,l) should be exactly on the Ewald sphere. Moreover, the direction of constructively diffracted wave is simply given by the vector pointing from the center of the crystal to that reciprocal-space grid point with coordinates (h,k,l). Hence, the Ewald sphere is quite a useful tool to determine the diffraction directions. The

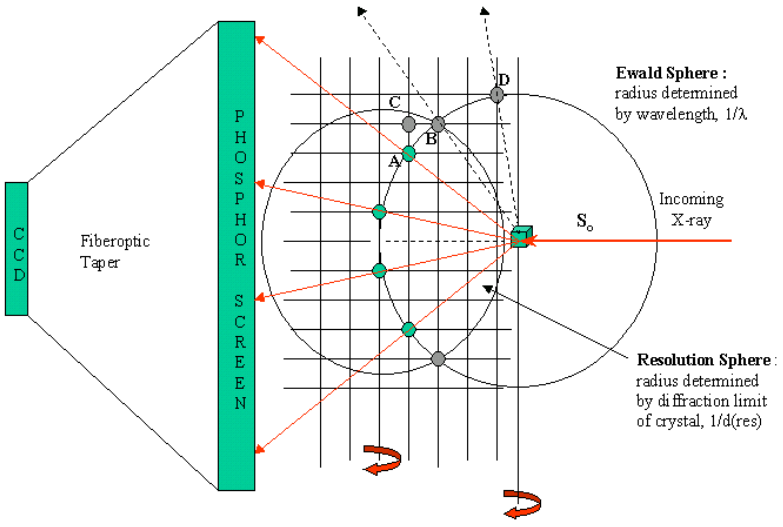

Figure 2.2. Ewald Sphere and Reciprocal Space [33].

quantities measured on the sensor screen is the square magnitude of structure factors, denoted by $|F_{hkl}|^2$ for the reflection planes with index (h,k,l). It can be shown [10]

that the crystal structure and structure factors are a *Continuous Fourier Series* pair (See (2.3) and (2.4))

$$\rho(x,y,z) = \frac{1}{XYZ}\sum_{hkl} F_{hkl} e^{-j2\pi(h\frac{x}{X}+k\frac{y}{Y}+l\frac{z}{Z})} \tag{2.3}$$

$$F_{hkl} = \iiint_V \rho(x,y,z) e^{j2\pi(h\frac{x}{X}+k\frac{y}{Y}+l\frac{z}{Z})} dx\, dy\, dz, \tag{2.4}$$

where $\rho(x,y,z)$ is the electron density at position vector $\vec{r} = (x,y,z)$ and X, Y, Z are the lengths of a unit cell's edges.

Literally, (2.3) requires a summation over all of the reciprocal-space grid points, i.e. all the (h,k,l) combinations. Technically, this is restricted. Although we can rotate the crystal such that the reciprocal-space grid is also rotating, forcing new grid points to arrive at the sphere, there is still limitation since the diffraction pattern should be detected by a sensor screen. As a result, there are only finite number structure factors, F_{hkl}, being recorded, and in this case, the electron density calculated using (2.3) will not be accurate. As shown in Fig. 2.2, there exits a limiting sphere containing all the reciprocal-space grid points having detectable structure factors. The limiting sphere is centered at the origin of the reciprocal space with the radius $1/D_{min}$ as shown in (2.5), where D_{min} is the minimum spacing between reflection planes. This spacing is also referred to as resolution distance and usually on the order of Å. For example, if the resolution of an electron density map is 2Å, r_ℓ is 1/2, as in

$$r_\ell = \frac{1}{D_{min}}. \tag{2.5}$$

2.2 Electron Cloud and Electron Density Map

As discussed in Section 1.2, a simplified model of the electron cloud (Fig. 2.3) will be used, which assumes a spherical Gaussian distribution [8][4][45].

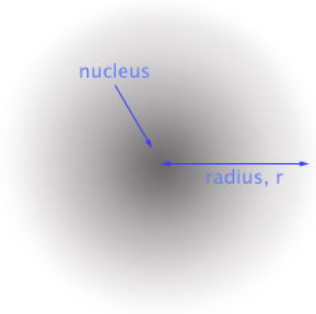

Figure 2.3. Spherical Gaussian Electron Cloud [14].

For $atom_i$, we denote the number of electrons in this atom by n_i, the coordinates of the atomic nuclei by x_i, y_i, z_i, and σ_{xi}, σ_{yi}, σ_{zi} represent the standard variance of the Gaussian distribution in x, y, z directions of a Cartesian coordinates system, assuming the distribution along all three directions are independent. Since the electron cloud is assumed spherical, $\sigma_{xi} = \sigma_{yi} = \sigma_{zi} = \sigma_i$. For a molecule composed of N atoms, we have the number of electrons at each point $\vec{r} = (x, y, z)$ provided by

$$\rho(x,y,z) = \sum_{i=1}^{N} n_i \cdot \frac{1}{\sqrt{2\pi}\sigma_i} e^{-\frac{(x-x_i)^2}{2\sigma_i^2}} \cdot \frac{1}{\sqrt{2\pi}\sigma_i} e^{-\frac{(y-y_i)^2}{2\sigma_i^2}} \cdot \frac{1}{\sqrt{2\pi}\sigma_i} e^{-\frac{(z-z_i)^2}{2\sigma_i^2}}, \quad (2.6)$$

where n_i means the number of electrons of the ith atom. (2.6) is suited to a N-atom system, where the standard variance σ_i is defined as atomic thermal factors. (2.6) was first introduced by Diamond [8] as a widely used Gaussian-distributed atomic model, which is also a resolution-independent EDM.

Due to the truncation error in the experiment, the measured structure factors are those confined in a *limiting sphere*. Thus, the so-constructed EDM in the above form is a blurred version of the original EDM. To calculate the modeled EDM regarding the resolution limitation, we thus compute the structure factors by substituting (2.6) into (2.4). The Fourier series synthesis (2.3) is then utilized with the summation over the (h, k, l)'s inside the limiting sphere. We denote the set of (h, k, l)'s pertaining to the measurable structure factors by Ω.

2.3 Resolution-dependent Electron Density Model

In this section, we derive a method for computing the local resolution-dependent EDM given a local structural conformation (e.g. a side chain rotamer). Specifically,

given the local structural conformation, we can construct a resolution-independent EDM assuming the Gaussian-distributed atomic model described in Section 2.2. To obtain the resolution-dependent EDM, we reformulate the effect of the truncation of structure factors in X-ray, i.e. the limiting sphere, as a equivalent *spherical filter*. For the reason stated in Section 3.2, we use a *cubic filter* instead, which is imposed by throwing away the structure factors near the surface of the limiting sphere, hence forming a *limiting cube*. It is known from *Signal Processing* theory, that if the input signal goes through a filter, the output signal will be a convolution of both the input signal and the filter's impulse response. Similarly, by representing the limiting cube in terms of a cubic filter, the resolution-dependent EDM will just be a 3D convolution of the resolution-independent EDM with the cubic filter's impulse response, which is written in terms of *Sinc functions*. Since exactly computing a convolution involving Sinc functions is computationally intractable, we study approximations using the Riemann sums instead of the Riemann integrals, through which the asymptotic running time is considerably improved.

In the last paragraph of Section 2.2, we have seen the modeled EDM can be calculated through the CFS pair; however, since we have to compute the resolution-dependent EDM starting from the resolution-independent EDM, it is desired to carry it out in the real space. By including the concept of filter, we can easily translate the reciprocal-space multiplication into a real-space convolution.

Since the reciprocal space is equivalent to the frequency domain in Fourier analysis, we consider the truncation of structure factors in reciprocal space as a *filter*. The most straightforward and physical way to truncate structure factors is to use the limiting sphere .

Due to the resolution limitation, all of the measurable structure factors are distributed inside the limiting sphere with the set of (h, k, l)'s denoted by Ω. As a result, the practical electron density function involving D_{min} is rewritten from (2.3) as

$$\begin{aligned}\rho(x,y,z,D_{min}) &= \frac{1}{XYZ}\sum_{hkl\in\Omega} F_{hkl}e^{-j2\pi(h\frac{x}{X}+k\frac{y}{Y}+l\frac{z}{Z})} \\ &= \frac{1}{XYZ}\sum_{hkl} \hat{F}_{hkl}e^{-j2\pi(h\frac{x}{X}+k\frac{y}{Y}+l\frac{z}{Z})},\end{aligned} \tag{2.7}$$

where

$$\hat{F}_{hkl} = \begin{cases} F_{hkl}, & if\ (\frac{h}{X})^2+(\frac{k}{Y})^2+(\frac{l}{Z})^2 \le r_\ell^2 \\ 0, & \text{otherwise.}\end{cases} \tag{2.8}$$

For periodic signals, we can directly derive the *Continuous Fourier Transform* (CFT) based on the Fourier series. With regards to $\rho(x,y,z,D_{min})$ and $\rho(x,y,z)$ respectively, we have the following two CFT expressions:

$$\begin{aligned}\hat{F}_{CFT}(\Omega_x,\Omega_y,\Omega_z) &= \sum_{h,k,l} 2\pi\,\hat{F}_{hkl}\,\delta(\Omega_x - h\frac{2\pi}{X})\,\delta(\Omega_y - k\frac{2\pi}{Y})\,\delta(\Omega_z - l\frac{2\pi}{Z}) \\ &= \sum_{(h,k,l)\in\Omega} 2\pi\,F_{hkl}\,\delta(\Omega_x - h\frac{2\pi}{X})\,\delta(\Omega_y - k\frac{2\pi}{Y})\,\delta(\Omega_z - l\frac{2\pi}{Z})\end{aligned} \tag{2.9}$$

$$F_{CFT}(\Omega_x,\Omega_y,\Omega_z) = \sum_{h,k,l} 2\pi\,F_{hkl}\,\delta(\Omega_x - h\frac{2\pi}{X})\,\delta(\Omega_y - k\frac{2\pi}{Y})\,\delta(\Omega_z - l\frac{2\pi}{Z}). \tag{2.10}$$

If we consider $F_{CFT}(\Omega_x,\Omega_y,\Omega_z)$ to be the *input*, and $\hat{F}_{CFT}(\Omega_x,\Omega_y,\Omega_z)$ as the *output*, the effect of limiting the resolution is equivalent to a *spherical filter*, which means the filter's frequency response only allows the frequency components within the limiting sphere pass and completely stop the band outside of that sphere. The cutoff frequency is determined by the resolution distance as

$$\Omega_c = 2\pi\, r_\ell = \frac{2\pi}{D_{min}}, \tag{2.11}$$

where the second "=" uses (2.5). The so-defined spherical filter's transfer function is shown as

$$H(\Omega_x, \Omega_y, \Omega_z) = \begin{cases} 1, & if \sqrt{\Omega_x^2 + \Omega_y^2 + \Omega_z^2} \leq \Omega_c = 2\pi r_\ell \\ 0, & \text{otherwise,} \end{cases} \tag{2.12}$$

where $r_\ell = \frac{1}{D_{min}}$ is the radius of the limiting sphere, D_{min} is the minimum spacing between reflection planes, and $\Omega_x, \Omega_y, \Omega_z$ are on the same scale as $\frac{2\pi h}{X}$, $\frac{2\pi k}{Y}$, $\frac{2\pi l}{Z}$, respectively.

As a property of the Fourier transform, a multiplication in the frequency domain (i.e. reciprocal space) equivalently leads to a convolution in the time domain (i.e. real space). So the desired resolution-dependent EDM is the convolution of the original resolution-independent EDM with the inverse Fourier transform of the transfer function, called the filter's impulse response,

$$\rho(x, y, z, D_{min}) \quad = \quad \rho(x, y, z) \otimes h(x, y, z) \tag{2.13}$$

where $\rho(x, y, z, D_{min})$ is the resolution-dependent EDM, $\rho(x, y, z)$ is the resolution-independent EDM, $h(x, y, z)$ is the filter's impulse response, and "$\otimes$" indicates the 3D convolution.

The spherical filter's impulse response is discussed in [32] and [29], and named as the *G-function* for sphere. If we use the limiting cube rather than the limiting sphere, the corresponding cubic filter is thus defined as

$$\begin{aligned} H(\Omega_x, \Omega_y, \Omega_z) \quad &= \quad \begin{cases} 1, & if \ |\Omega_x|, |\Omega_y|, |\Omega_z| \leq \Omega_c = 2\pi \frac{r_\ell}{\sqrt{2}} < 2\pi r_\ell \\ 0, & otherwise \end{cases} \\ &= \quad rect(\frac{\Omega_x}{2\Omega_c}) \cdot rect(\frac{\Omega_y}{2\Omega_c}) \cdot rect(\frac{\Omega_z}{2\Omega_c}). \end{aligned} \tag{2.14}$$

The G-function for a cube is also derived in [32] and [29], as

$$h(x,y,z) = (\frac{\Omega_c}{\pi})^3 sinc(\frac{\Omega_c}{\pi}x)\, sinc(\frac{\Omega_c}{\pi}y)\, sinc(\frac{\Omega_c}{\pi}z), \tag{2.15}$$

which is illustrated in Fig. 2.4, below.

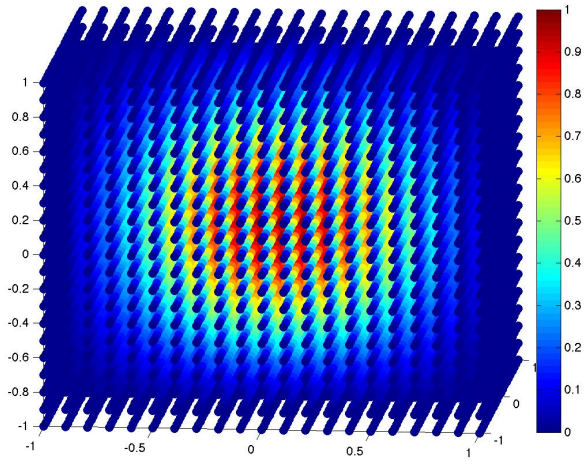

Figure 2.4. 3D Impulse Response Formed by Sinc Function

Substituting (2.6) and (2.15) into (2.13), we have

$$\begin{aligned}
\rho(x,y,z,D_{min}) &= \rho(x,y,z) \otimes (\frac{\Omega_c}{\pi})^3 sinc(\frac{\Omega_c}{\pi}x)\, sinc(\frac{\Omega_c}{\pi}y)\, sinc(\frac{\Omega_c}{\pi}z) \\
&= \sum_{i=1}^{N} n_i \cdot [\int_{-\infty}^{\infty} \frac{1}{\sqrt{2\pi}\sigma_x} e^{-\frac{(\tau - x_i)^2}{2\sigma_x^2}} (\frac{\Omega_c}{\pi}) sinc(\frac{\Omega_c}{\pi}(x-\tau))\, d\tau] \\
&\quad [\int_{-\infty}^{\infty} \frac{1}{\sqrt{2\pi}\sigma_y} e^{-\frac{(\tau - y_i)^2}{2\sigma_y^2}} (\frac{\Omega_c}{\pi}) sinc(\frac{\Omega_c}{\pi}(y-\tau))\, d\tau] \\
&\quad [\int_{-\infty}^{\infty} \frac{1}{\sqrt{2\pi}\sigma_z} e^{-\frac{(\tau - z_i)^2}{2\sigma_z^2}} (\frac{\Omega_c}{\pi}) sinc(\frac{\Omega_c}{\pi}(z-\tau))\, d\tau] \\
&\approx \sum_{i=1}^{N} n_i \cdot [\int_{-3\sigma_x}^{3\sigma_x} \frac{1}{\sqrt{2\pi}\sigma_x} e^{-\frac{(\tau)^2}{2\sigma_x^2}} (\frac{\Omega_c}{\pi}) sinc(\frac{\Omega_c}{\pi}(x - x_i - \tau))\, d\tau] \\
&\quad [\int_{-3\sigma_y}^{3\sigma_y} \frac{1}{\sqrt{2\pi}\sigma_y} e^{-\frac{(\tau)^2}{2\sigma_y^2}} (\frac{\Omega_c}{\pi}) sinc(\frac{\Omega_c}{\pi}(y - y_i - \tau))\, d\tau] \\
&\quad [\int_{-3\sigma_z}^{3\sigma_z} \frac{1}{\sqrt{2\pi}\sigma_z} e^{-\frac{(\tau)^2}{2\sigma_z^2}} (\frac{\Omega_c}{\pi}) sinc(\frac{\Omega_c}{\pi}(z - z_i - \tau))\, d\tau].
\end{aligned} \tag{2.16}$$

The final step of the above derivation comes from the change of variables and the *3σ Rule* of Gaussian variables [44]. Regarding to the three definite integrals in (2.16), we can replace the Riemann integrals with the Riemann sums as long as the partition of the integral interval becomes fine enough. If we take D_{min} to range from 1Å to 4Å, hence the parameter in the Sinc functions is given by, $\frac{\pi}{\Omega_c} = \frac{\pi D_{min}}{2\pi} = \frac{D_{min}}{2}$ or 0.5Å∼2Å. Furthermore, the width of the Gaussian functions is related to the atomic radius, i.e. $\sigma_x = \sigma_y = \sigma_z = 0.55$Å for a carbon atom, and likewise 0.6Å for a sulfur atom. It can be verified that each Riemann integral in (2.16) can be calculated precisely using a Riemann sum if the interval $[-3\sigma_{x(y,z)}, 3\sigma_{x(y,z)}]$ is divided into 8 subintervals, which we call the *8-division method*. We thus have a numerical way to compute the resolution-dependent EDM. To see the accuracy of this numerical result, we show 1D simulation of the Gaussian-distributed carbon atom with the atomic radius 0.55Å and 6 electrons around the nuclei, and then calculate the resolution-dependent EDM at resolution 1Å, 2Å and 4Å. The numerical result using the 8-division method is well consistent with the exact solution given by the direct numerical integral (see Fig. 2.5, Fig. 2.6 and Fig. 2.7).

This section addressed a method to build the EDM model analytically as opposed to the observed EDM. This *forward model* is important for the *Maximum Likelihood* (ML) formulation, since to maximize the likelihood function is to minimize the difference between the observation and the theoretical model while taking into account the observational variance.

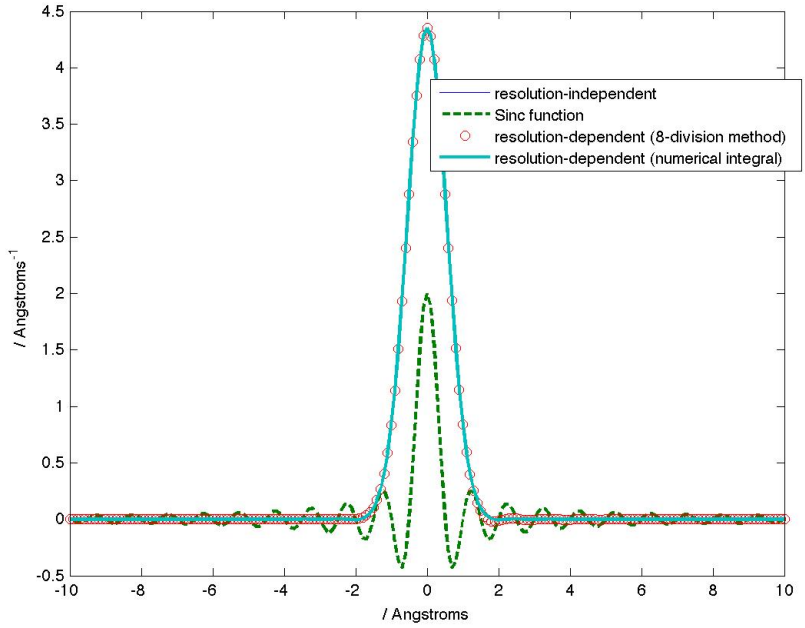

Figure 2.5. 8-division method vs. direct numerical integral in the 1D simulation of resolution-dependent EDM for a carbon atom at 1Å

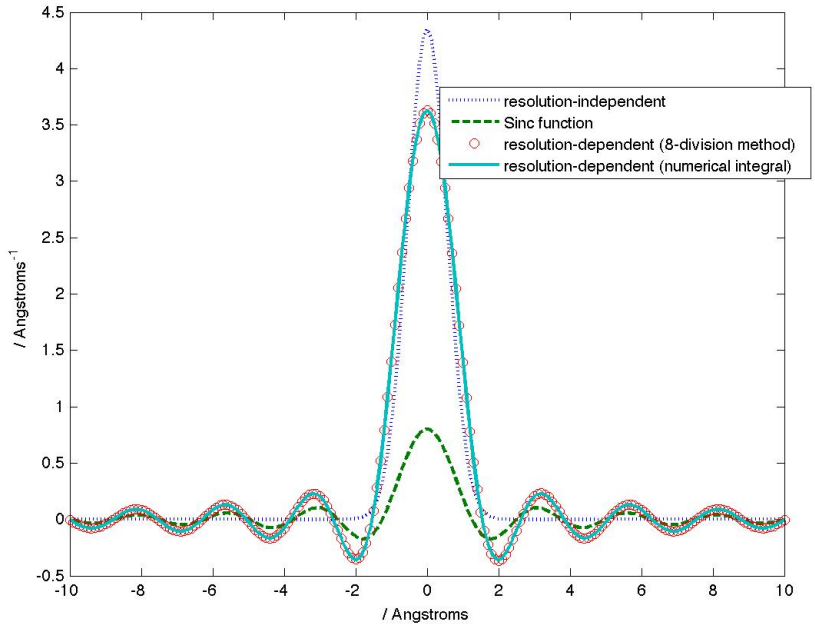

Figure 2.6. 8-division method vs. direct numerical integral in the 1D simulation of resolution-dependent EDM for a carbon atom at 2.5Å

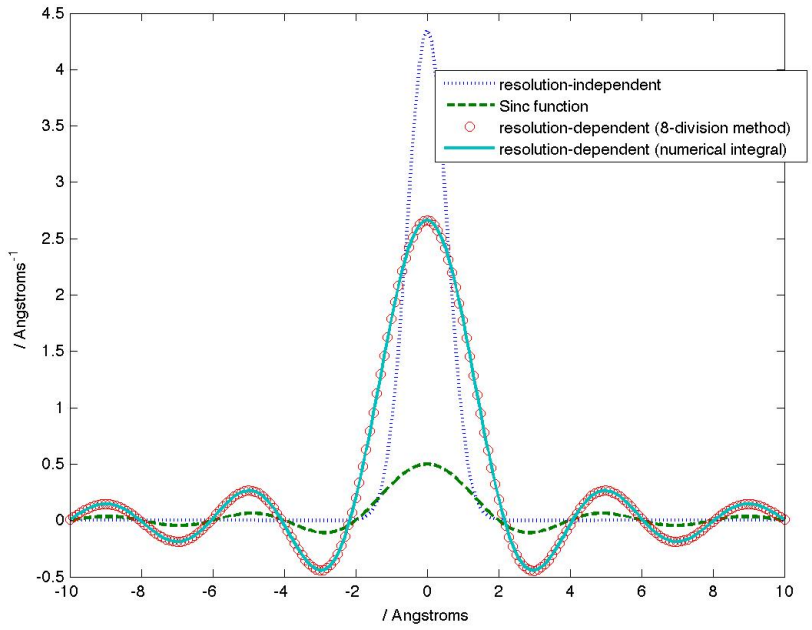

Figure 2.7. 8-division method vs. direct numerical integral in the 1D simulation of resolution-dependent EDM for a carbon atom at 4Å

CHAPTER 3

ERROR DISTRIBUTION OF RESOLUTION-DEPENDENT ELECTRON DENSITIES

Regarding the side chain assignment using X-ray data, we must always choose the best-fit side chain conformation from a number of choices (e.g. rotamers). To score each choice, we should compare the modeled resolution-dependent EDM (see Section 2.3) against the observed EDM according to some particular error distribution.

In Section 3.1, we use DFT to represent the relationship between structure factors and electron density values. Although continuous Fourier series (CFS) is widely used to compute an EDM from observed structure factors, we use the DFT relationship in a novel way to also compute the error propagation from observed structure factors to the resolution-dependent electron density values.

When we perform a DFT, sampling the continuous electron density function to a discrete one will create periodic replicas of the original spectrum repeated at the reciprocal-space grid points, resulting in aliasing or overlapping of the spectrum in the reciprocal domain. So, working with a DFT without aliasing requires us to choose the sampling frequency to at least the Nyquist's frequency. However, if the sampling frequency is too high, we will see in Section 3.2, there will be many redundant zeros in the reciprocal space, correlating the electron density values at different points in the real space. To address aliasing and also avoid correlation between resolution-dependent electron density values, we require two steps: first, we choose the sampling frequency to be the Nyquist frequency, and second, we use a cubic filter as described

in (2.14). Then, by assuming all the real and imaginary parts of the structure factors are *independent and identically-distributed* (i.i.d.) Gaussian and noting DFT is a unitary transformation, we conclude the measured resolution-dependent electron density values are i.i.d. Gaussian as well. This property in turn, transforms the local structure refinement into a maximum-likelihood problem that can be solved by least squares (Section 3.3). Finally, in Section 3.4, we perform decision-makings for SCA problem using X-ray data only, and present the calculation of the confidence probability.

3.1 Discrete Fourier Transform (DFT) Representation

The well known relationships (2.3) and (2.4) between electron densities and structure factors are rewritten by the following formula pair:

$$\rho(x,y,z) = \frac{1}{XYZ}\sum_{hkl} F_{hkl} e^{-j2\pi(h\frac{x}{X}+k\frac{y}{Y}+l\frac{z}{Z})} \tag{3.1}$$

$$F_{hkl} = \iiint_V \rho(x,y,z) e^{j2\pi(h\frac{x}{X}+k\frac{y}{Y}+l\frac{z}{Z})} dx\, dy\, dz \tag{3.2}$$

where $\rho(x,y,z)$ is the electron density at position vector $\vec{r} = (x,y,z)$ and X, Y, Z are the lengths of the unit cell's edges.

This representation is conventionally known as discrete Fourier transform (DFT) [6]. Here we will clarify the confusion between continuous Fourier series (CFS) and DFT. The crystal can be considered as a convolution of one unit cell's electron density function and a lattice of delta functions, with the spacing between lattice grid points being equal to the dimension of unit cell. The real-space convolution implies a reciprocal-space multiplication. Once the product of the two Fourier domain components is obtained, by applying inverse Fourier transform, we have the above (3.1). The inclusion of 3D lattice makes the summation look like a DFT. However, by referring to the theory of *Digital Signal Processing* (DSP), we know that (3.1) and (3.2)

are respectively the synthetic and analytic equations of *Continuous Fourier Series* (CFS). In fact, the sampled or discretized lattice in CFS is over the 3D crystal, while the DFT sampling grid is within a single unit cell of the given crystal. That is the fundamental difference between these two concepts.

In DSP theory, (3.1) and (3.2) are the standard definitions of 3D CFS. The exact definitions of *Continuous Fourier Transform* (CFT) is given in (3.3), *Discrete-time Fourier Transform* (DTFT) in (3.4), and *Discrete Fourier Transform* (DFT) in (3.6) as follows.

$$\begin{aligned} \rho(x,y,z) &= \frac{1}{XYZ}\frac{1}{(2\pi)^3}\iiint F_{CFT}(\Omega_x,\Omega_y,\Omega_z)e^{-j(\Omega_x\,x+\Omega_y\,y+\Omega_z\,z)}\,d\Omega_x\,d\Omega_y\,d\Omega_z \\ F_{CFT}(\Omega_x,\Omega_y,\Omega_z) &= XYZ\iiint \rho(x,y,z)e^{j(\Omega_x\,x+\Omega_y\,y+\Omega_z\,z)}dx\,dy\,dz \end{aligned} \tag{3.3}$$

$$\begin{aligned} \rho[n_x,n_y,n_z] &= \frac{1}{XYZ}\frac{1}{(2\pi)^3}\iiint F_{DTFT}(\omega_x,\omega_y,\omega_z)e^{-j(\omega_x\,n_x+\omega_y\,n_y+\omega_z\,n_z)}\,d\omega_x\,d\omega_y\,d\omega_z \\ F_{DTFT}(\omega_x,\omega_y,\omega_z) &= XYZ\sum_{n_x=-\infty}^{\infty}\sum_{n_y=-\infty}^{\infty}\sum_{n_z=-\infty}^{\infty}\rho[n_x,n_y,n_z]e^{j(\omega_x\,n_x+\omega_y\,n_y+\omega_z\,n_z)} \end{aligned} \tag{3.4}$$

$$\begin{aligned} \rho[n_x,n_y,n_z] &= \frac{1}{XYZ}\frac{1}{N_xN_yN_z}\sum_{k_x=0}^{N_x-1}\sum_{k_y=0}^{N_y-1}\sum_{k_z=0}^{N_z-1}F_{DFT}[k_x,k_y,k_z]e^{-j(\frac{2\pi k_x\,n_x}{N_x}+\frac{2\pi k_y\,n_y}{N_y}+\frac{2\pi k_z\,n_z}{N_z})} \\ F_{DFT}[k_x,k_y,k_z] &= XYZ\sum_{n_x=0}^{N_x-1}\sum_{n_y=0}^{N_y-1}\sum_{n_z=0}^{N_z-1}\rho[n_x,n_y,n_z]e^{j(\frac{2\pi k_x\,n_x}{N_x}+\frac{2\pi k_y\,n_y}{N_y}+\frac{2\pi k_z\,n_z}{N_z})} \end{aligned} \tag{3.5}$$

where $\rho[n_x,n_y,n_z]=\rho(n_x\Delta x,n_y\Delta y,n_z\Delta z)$ is the sampled discrete version of the continuous function, $\rho(x,y,z)$, and $\Delta x,\Delta y,\Delta z$ are the sampling intervals along $x-$, $y-$, $z-$ axes. By definition, we have $\Delta x=\frac{X}{N_x}$, and similarly for Δy and Δz. It is clear from the above formulation that the summation in DFT is different from the one in CFS.

Note all the above equations are defined for the resolution-independent EDM. As for the resolution-dependent EDM, these relationships are the same except that the structure factors are truncated by the limiting sphere/cube. Because the discrete resolution-dependent EDM can easily be stored in digital devices as a discrete function over 3D grid, it is desirable to study the relationship between structure factors and electron density values in a discrete case, i.e. the DFT representation. Furthermore, the DFT can be implemented efficiently using an FFT.

$$\rho[n_x, n_y, n_z, D_{min}] = \frac{1}{XYZ}\frac{1}{N_xN_yN_z}\sum_{k_x=0}^{N_x-1}\sum_{k_y=0}^{N_y-1}\sum_{k_z=0}^{N_z-1}\hat{F}_{DFT}[k_x, k_y, k_z]e^{-j(\frac{2\pi k_x\, n_x}{N_x}+\frac{2\pi k_y\, n_y}{N_y}+\frac{2\pi k_z\, n_z}{N_z})}$$

$$\hat{F}_{DFT}[k_x, k_y, k_z] = XYZ\sum_{n_x=0}^{N_x-1}\sum_{n_y=0}^{N_y-1}\sum_{n_z=0}^{N_z-1}\rho[n_x, n_y, n_z, D_{min}]e^{j(\frac{2\pi k_x\, n_x}{N_x}+\frac{2\pi k_y\, n_y}{N_y}+\frac{2\pi k_z\, n_z}{N_z})} \tag{3.6}$$

where $\rho[n_x, n_y, n_z, D_{min}]$ is the sampled discrete version of the continuous function, $\rho(x, y, z, D_{min})$, and the symbol "$\hat{}$" represents that the DFT coefficients are related to the convolved resolution-dependent EDM, $\rho(x, y, z, D_{min})$, as defined in (2.7) and numerically computed by (2.16).

The resolution-dependent electron density function is 3D periodic over the crystal. We already have its CFS given in (2.8), and CFT in (2.9). After sampling, $\rho(x, y, z, D_{min})$ is discretized to $\rho[n_x, n_y, n_z, D_{min}]$, and thus can be used to compute DTFT and DFT.

From DSP theory, we have the following relationships between Fourier transforms and Fourier series:

$$\hat{F}_{CFT}(\Omega_x, \Omega_y, \Omega_z) = \sum_{h=-\infty}^{\infty}\sum_{k=-\infty}^{\infty}\sum_{l=-\infty}^{\infty}(2\pi)^3\,\hat{F}_{hkl}\delta(\Omega_x - h\frac{2\pi}{X})\delta(\Omega_y - k\frac{2\pi}{Y})\delta(\Omega_z - l\frac{2\pi}{Z}) \tag{3.7}$$

$$\hat{F}_{DTFT}(\omega_x,\omega_y,\omega_z)=\frac{1}{\Delta x\Delta y\Delta z}\sum_{h=-\infty}^{\infty}\sum_{k=-\infty}^{\infty}\sum_{l=-\infty}^{\infty}\hat{F}_{CFT}(\frac{\omega_x-2\pi h}{\Delta x},\frac{\omega_y-2\pi k}{\Delta y},\frac{\omega_z-2\pi l}{\Delta z}) \tag{3.8}$$

$$\hat{F}_{DTFT}(\omega_x,\omega_y,\omega_z)=\sum_{h=-\infty}^{\infty}\sum_{k=-\infty}^{\infty}\sum_{l=-\infty}^{\infty}\frac{(2\pi)^3}{N_xN_yN_z}\hat{F}_{DFT}[h,k,l]\delta(\omega_x-h\frac{2\pi}{N_x})\delta(\omega_y-k\frac{2\pi}{N_y})\delta(\omega_z-l\frac{2\pi}{N_z}) \tag{3.9}$$

Substituting (3.7) into (3.8) and comparing with (3.9), the relationship between CFS and DFT can be written as

$$\hat{F}_{DFT}[h,k,l]=N_xN_yN_z\sum_{m=-\infty}^{\infty}\hat{F}_{(h+mN_x)(k+mN_y)(l+mN_z)}, \tag{3.10}$$

where "$\hat{}$" means the structure factors are truncated by the limiting sphere as in (3.6). Specifically, for the spherical filter,

$$\hat{F}_{hkl}=\begin{cases}F_{hkl}, & if\ (\frac{h}{X})^2+(\frac{k}{Y})^2+(\frac{l}{Z})^2\le r_\ell^2\\ 0, & \text{otherwise;}\end{cases} \tag{3.11}$$

while for a cubic filter,

$$\hat{F}_{hkl}=\begin{cases}F_{hkl}, & if\ |\frac{h}{X}|,|\frac{k}{Y}|,|\frac{l}{Z}|\le\frac{r_\ell}{\sqrt{2}}<r_\ell\\ 0, & \text{otherwise.}\end{cases} \tag{3.12}$$

The problem of aliasing appears apparently in (3.10), which was first demonstrated for reciprocal-space structure refinements in [4] and [28]. To avoid aliasing, an imaginary thermal factor, i.e. B-factor, is included to make the spectrum shrink. In our problem, the reciprocal-space components, $\hat{F}_{hkl}$'s, are already truncated by the

limiting sphere as in (2.12). As long as we make the sampling grid fine enough, those infinitely many periodic replicas of $\hat{F}_{hkl}$ cannot overlap. In other words, the sampling frequency should satisfy Nyquist's criterion, given by

$$\begin{aligned} \Omega_c \cdot \Delta x &\leq \pi \\ \Omega_c \cdot \Delta y &\leq \pi \\ \Omega_c \cdot \Delta z &\leq \pi \end{aligned} \tag{3.13}$$

or

$$\begin{aligned} \Delta x &\leq \frac{D_{min}}{2} \\ \Delta y &\leq \frac{D_{min}}{2} \\ \Delta z &\leq \frac{D_{min}}{2} \end{aligned} \tag{3.14}$$

for the limiting sphere and

$$\begin{aligned} \Delta x &\leq \frac{D_{min}}{\sqrt{2}} \\ \Delta y &\leq \frac{D_{min}}{\sqrt{2}} \\ \Delta z &\leq \frac{D_{min}}{\sqrt{2}} \end{aligned} \tag{3.15}$$

for the limiting cube.

Furthermore, if the sampling frequency is greater than or equal to the Nyquist's frequency, which is the least one to avoid the overlapping of spectrum, (3.10) can be simplified as

$$\hat{F}_{DFT}[h,k,l] = N_x N_y N_z \, \hat{F}_{h'k'l'} \tag{3.16}$$

where $h' = \begin{cases} h, & if\ h < N_x - h \\ h - N_x, & otherwise, \end{cases}$ $k' = \begin{cases} k, & if\ k < N_y - k \\ k - N_y, & otherwise, \end{cases}$

$l' = \begin{cases} l, & if\ l < N_z - l \\ l - N_z, & otherwise. \end{cases}$

Note for the DFT, h, k, l are integers from the intervals $[0, N_x - 1], [0, N_y - 1], [0, N_z - 1]$ respectively.It should also be noted that $\hat{F}_{h'k'l'}$ are either measured structure factors, or constant zeros added when performing 3D DFT.

Substituting (3.16) into (3.6), we have

$$\rho[n_x, n_y, n_z, D_{min}] = \frac{1}{XYZ} \sum_{h=0}^{N_x-1} \sum_{k=0}^{N_y-1} \sum_{l=0}^{N_z-1} \hat{F}_{h'k'l'} e^{-j(\frac{2\pi h\, n_x}{N_x} + \frac{2\pi k\, n_y}{N_y} + \frac{2\pi l\, n_z}{N_z})} \tag{3.17}$$

$$\hat{F}_{h'k'l'} = \frac{XYZ}{N_x N_y N_z} \sum_{n_x=0}^{N_x-1} \sum_{n_y=0}^{N_y-1} \sum_{n_z=0}^{N_z-1} \rho[n_x, n_y, n_z, D_{min}] e^{j(\frac{2\pi h\, n_x}{N_x} + \frac{2\pi k\, n_y}{N_y} + \frac{2\pi l\, n_z}{N_z})}, \tag{3.18}$$

and then put (3.18) in a matrix form as

$$\underline{\hat{F}} = \frac{XYZ}{N_x\, N_y\, N_z} E \ \ \underline{\hat{\rho}} = \frac{1}{\sqrt{N_x\, N_y\, N_z}} (\frac{1}{\sqrt{N_x\, N_y\, N_z}} E)\ XYZ\ \underline{\hat{\rho}}\ , \tag{3.19}$$

where $\underline{\hat{F}}$ and $\underline{\hat{\rho}}$ are column vectors including the real and imaginary parts of all of the $\hat{F}_{h'k'l'}$'s and $\rho[n_x, n_y, n_z, D_{min}]$'s respectively for $0 \le n_x(h) \le N_x - 1$, $0 \le n_y(k) \le N_y - 1$, $0 \le n_z(l) \le N_z - 1$. E is a $2N_xN_yN_z \times 2N_xN_yN_z$ matrix, which is composed of the real and imaginary parts of all the complex exponentials. It can be shown that $(\frac{1}{\sqrt{N_x\, N_y\, N_z}} E)$ is a unitary matrix, denoted as A. Then a property of a unitary matrix follows, i.e. $A^T A = AA^T = I$, where I is an identity matrix. (3.19) can be rewritten as

$$\underline{\hat{F}} = \frac{XYZ}{\sqrt{N_x\, N_y\, N_z}} A \ \ \underline{\hat{\rho}}\ . \tag{3.20}$$

To verify that matrix $(\frac{1}{\sqrt{N_x\,N_y\,N_z}}E)$ is a unitary matrix, we write down all the entries of this matrix. A unitary matrix has any pair of different rows orthogonal and the squared norm of each row equal to one. So we can check the inner product of any pair of rows, say one row with index tuple (h,k,l), and the other with (H,K,L). They can be the same, and in that case, these two rows describe a single row. It is easy to see the inner product actually fall into two categories. Let r and r' represent two rows. Suppose both of them correspond to the real (imaginary) parts of two complex structure factors, we have the inner product given as

$$
\begin{aligned}
& \frac{1}{N_x\,N_y\,N_z}\sum_{n_x=0}^{N_x-1}\sum_{n_y=0}^{N_y-1}\sum_{n_z=0}^{N_z-1}[cos(\frac{2\pi h\,n_x}{N_x}+\frac{2\pi k\,n_y}{N_y}+\frac{2\pi l\,n_z}{N_z})\ cos(\frac{2\pi H\,n_x}{N_x}+\frac{2\pi K\,n_y}{N_y}+\frac{2\pi L\,n_z}{N_z}) \\
& +sin(\frac{2\pi h\,n_x}{N_x}+\frac{2\pi k\,n_y}{N_y}+\frac{2\pi l\,n_z}{N_z})\ sin(\frac{2\pi H\,n_x}{N_x}+\frac{2\pi K\,n_y}{N_y}+\frac{2\pi L\,n_z}{N_z})] \\
= & \frac{1}{N_x\,N_y\,N_z}\sum_{n_x=0}^{N_x-1}\sum_{n_y=0}^{N_y-1}\sum_{n_z=0}^{N_z-1}cos(2\pi n_x\frac{h-H}{N_x}+2\pi\,n_y\frac{k-K}{N_y}+2\pi\,n_z\frac{l-L}{N_z}) \\
= & \frac{1}{N_x\,N_y\,N_z}\Re[\sum_{n_x=0}^{N_x-1}\sum_{n_y=0}^{N_y-1}\sum_{n_z=0}^{N_z-1}e^{j2\pi n_x\frac{h-H}{N_x}+j2\pi\,n_y\frac{k-K}{N_y}+j2\pi\,n_z\frac{l-L}{N_z}}] \\
= & \frac{1}{N_x\,N_y\,N_z}\Re[\sum_{n_x=0}^{N_x-1}e^{j2\pi n_x\frac{h-H}{N_x}}\sum_{n_y=0}^{N_y-1}e^{j2\pi\,n_y\frac{k-K}{N_y}}\sum_{n_z=0}^{N_z-1}e^{j2\pi\,n_z\frac{l-L}{N_z}}] \\
= & \begin{cases} 1, & if\ h=H,k=K,l=L \\ 0, & otherwise. \end{cases}
\end{aligned}
\tag{3.21}
$$

If r and r' are from the same structure factor, the inner product is one; otherwise, it is zero.

In the other case, when we have one row from the real part of a structure factor, and the other row from the imaginary part of a structure factor, we have

$$
\begin{aligned}
& \frac{1}{N_x\,N_y\,N_z}\sum_{n_x=0}^{N_x-1}\sum_{n_y=0}^{N_y-1}\sum_{n_z=0}^{N_z-1}[sin(\frac{2\pi h\,n_x}{N_x}+\frac{2\pi k\,n_y}{N_y}+\frac{2\pi l\,n_z}{N_z})\ cos(\frac{2\pi H\,n_x}{N_x}+\frac{2\pi K\,n_y}{N_y}+\frac{2\pi L\,n_z}{N_z}) \\
& -cos(\frac{2\pi h\,n_x}{N_x}+\frac{2\pi k\,n_y}{N_y}+\frac{2\pi l\,n_z}{N_z})\ sin(\frac{2\pi H\,n_x}{N_x}+\frac{2\pi K\,n_y}{N_y}+\frac{2\pi L\,n_z}{N_z})] \\
= & \frac{1}{N_x\,N_y\,N_z}\sum_{n_x=0}^{N_x-1}\sum_{n_y=0}^{N_y-1}\sum_{n_z=0}^{N_z-1} sin(2\pi n_x\frac{h-H}{N_x}+2\pi\,n_y\frac{k-K}{N_y}+2\pi\,n_z\frac{l-L}{N_z}) \\
= & \frac{1}{N_x\,N_y\,N_z}\Im[\sum_{n_x=0}^{N_x-1}\sum_{n_y=0}^{N_y-1}\sum_{n_z=0}^{N_z-1} e^{j2\pi n_x\frac{h-H}{N_x}+j2\pi\,n_y\frac{k-K}{N_y}+j2\pi\,n_z\frac{l-L}{N_z}}] \\
= & \frac{1}{N_x\,N_y\,N_z}\Im[\sum_{n_x=0}^{N_x-1} e^{j2\pi n_x\frac{h-H}{N_x}}\sum_{n_y=0}^{N_y-1} e^{j2\pi\,n_y\frac{k-K}{N_y}}\sum_{n_z=0}^{N_z-1} e^{j2\pi\,n_z\frac{l-L}{N_z}}] \\
= & 0, \qquad (3.22)
\end{aligned}
$$

which implies the inner product is constant zero no matter whether they are from the same structure factor.

From both the cases mentioned above, we conclude the $2N_xN_yN_z$ rows are orthonormal, so the square matrix $(\frac{1}{\sqrt{N_x\,N_y\,N_z}}E)$ is a unitary matrix.

3.2 The Probability Distribution of Electron Densities

It is seen that by choosing sampling frequency greater than or equal to the Nyquist's frequency, the discrete electron densities calculated from the DFT synthetic equation (3.17) are exactly the sampled values of the continuous resolution-dependent EDM given in (2.7). We assume the observed complex structure factors are i.i.d. 2D Gaussian-distributed; however, as shown later, the discrete electron densities are also i.i.d. 2D Gaussian as long as there is no constant zero in the column vector, $\underline{\hat{F}}$. Based on this requirement, the limiting sphere is discarded and a limiting cube along with its implementation is presented.

The deterministic equation (3.20) can be taken as a modeled relationship, which is overwritten as

$$\underline{\hat{F}}_{cal} = \frac{XYZ}{\sqrt{N_x\, N_y\, N_z}} A \;\; \underline{\hat{\rho}}_{cal} \; . \tag{3.23}$$

Let us consider a random scenario, which requires to study the joint probabilistic distribution of the random vector, consisting of the measured structure factors, denoted as $\underline{\hat{F}}_{obs}$, meaning the observed random vector.

The general distribution of individual structure factors is given by Read [30]. The conditional error distribution of a particular structure factor given a structural model relies on both the model's coordinate errors and the contributions from the missing atoms. The general distribution is a 2D Gaussian distribution, given by

$$\hat{F}_{hkl_{obs}} = D(h,k,l,D_{min}) \; \hat{F}_{hkl_{cal}} + \epsilon \; , \tag{3.24}$$

where ϵ is a 2D Gaussian error. The mean value is

$$\langle \hat{F}_{hkl_{obs}} \rangle = D(h,k,l,D_{min}) \; \hat{F}_{hkl_{cal}} \; .$$

The real and imaginary parts of ϵ are independent and identical-distributed (i.i.d.) 1D Gaussian random variables, with the variances equal to

$$\sigma_F^2 = [1 - D^2(h,k,l,D_{min})]\Sigma_P + \Sigma_Q,$$

where Σ_P and Σ_Q represent the variance contributions from the known atoms in the given model, and the missing atoms (e.g. water molecules in our problem) to be determined, respectively. $D(h,k,l,D_{min})$ can be complex, which implies the coordinate errors of the known atoms in the model. One more note is made here that $D(h,k,l,D_{min})$ in Read's work [30] is a function of the resolution, D_{min}, and the reciprocal-space coordinates, (h,k,l); however, if the resolution-dependent EDM in Section 2.3 is used, $D(h,k,l,D_{min})$ is not varying with the resolution.

We focus on the ML estimate of the structural conformations, which always maximizes the conditional probability of the observed data given the modeled structure, meaning the structure is perfectly known. Also, we assume the thermal motion of the native structure in the crystal can be ignored, compared with the wide-type structural dynamics. For these reasons, we take the atomic model for calculating modeled structure factors as a perfect one, and all of the atomic coordinate errors can thus be eliminated, which gives $D(h,k,l,D_{min}) \approx 1$. Then (3.24) is simplified as

$$\hat{F}_{hkl_{obs}} = \hat{F}_{hkl_{cal}} + \epsilon \tag{3.25}$$

with the mean $\langle \hat{F}_{hkl_{obs}} \rangle = \hat{F}_{hkl_{cal}}$ and the variance $\sigma_F^2 = \Sigma_Q$, which implies the random errors, ϵ's, for different structure factors, are identically-distributed 2D Gaussian complex random variables with zero-mean and σ_F^2 as the variance.

Next, we take a look at the joint probability distribution of a set of structure factors. Klug [23] find out that the cross-correlated terms of the joint distribution are proportional to $N^{-1/2}$, where N is the number of atoms in the system. For large molecules (e.g. proteins), containing much more than hundreds of atoms, the correlations between different structure factors become so weak that they can be neglected without involving much error.

Thus, given the calculated structure factors from a structural model, the real and imaginary parts of the measured structure factors can be considered as an *independent and identically-distributed* (i.i.d.) Gaussian random vector. The general distribution is given as

$$\underline{\hat{F}}_{obs} = \underline{\hat{F}}_{cal} + \underline{\epsilon} \ , \tag{3.26}$$

where $\underline{\epsilon}$ is a $2N_xN_yN_z$ by 1 random vector comprising with i.i.d. Gaussian entries having zero mean, variance σ_F^2, along with constant zeros depending on the choice of

sampling frequency. Note $\underline{\epsilon}$ is but a real vector since we put all the real and imaginary parts of the structure factors in a vector form.

Substituting (3.23) into (3.26),

$$\begin{aligned} \underline{\hat{F}}_{obs} &= \frac{XYZ}{\sqrt{N_x\, N_y\, N_z}} A \;\; \underline{\hat{\rho}}_{cal} + \underline{\epsilon} \\ &= B \;\; \underline{\hat{\rho}}_{cal} + \underline{\epsilon} \end{aligned} \tag{3.27}$$

where $B = \frac{XYZ}{\sqrt{N_x\, N_y\, N_z}} A$.

The least squares (LS) estimate of $\underline{\hat{\rho}}_{cal}$ is denoted as $\underline{\hat{\rho}}_{obs}$, and given by

$$\begin{aligned} \underline{\hat{\rho}}_{obs} &= (B^T B)^{-1} B^T \underline{\hat{F}}_{obs} \\ &= \frac{\sqrt{N_x\, N_y\, N_z}}{XYZ} A^T \underline{\hat{F}}_{obs} \end{aligned} \tag{3.28}$$

where $A^T A = I$ is used.

So, according to (3.28), an observed EDM can be constructed based on the measured complex structure factors. Here it should be pointed out, the state-of-the-art techniques can not only measure the amplitudes of structure factors, but also the phase information through *multiple isomorphous replacement* (MIR) or *multi-wavelength anomalous diffraction* (MAD) [31][2], which renews the general interest in real-space refinement. Since the phase information is measured precisely, we are not restricted to refine the amplitudes of structure factors in the reciprocal space. Without mention of the phase measurements, for the rest of this thesis, we assume the phase information is measured through either MIR or MAD.

(3.28) shows that the LS estimate $\underline{\hat{\rho}}_{obs}$ is a linear transformation of $\underline{\hat{F}}_{obs}$, which consists of i.i.d. Gaussian structure factors and constant zeros (i.e. Gaussian with zero mean, zero variance). So we conclude the random vector $\underline{\hat{\rho}}_{obs}$ is Gaussian as well. To describe a Gaussian random vector, there are two parameters: the mean vector and the covariance matrix.

The mean vector of $\underline{\hat{\rho}}_{obs}$ is

$$\begin{aligned}
\langle \underline{\hat{\rho}}_{obs} \rangle &= \frac{\sqrt{N_x\, N_y\, N_z}}{XYZ} A^T \langle \underline{\hat{F}}_{obs} \rangle \\
&= \frac{\sqrt{N_x\, N_y\, N_z}}{XYZ} A^T \frac{XYZ}{\sqrt{N_x\, N_y\, N_z}} A\ \underline{\hat{\rho}}_{cal} \\
&= \underline{\hat{\rho}}_{cal}\ , \qquad (3.29)
\end{aligned}$$

and the covariance matrix is given by

$$\begin{aligned}
\Sigma &= E[(\underline{\hat{\rho}}_{obs} - \langle \underline{\hat{\rho}}_{obs} \rangle)(\underline{\hat{\rho}}_{obs} - \langle \underline{\hat{\rho}}_{obs} \rangle)^T] \\
&= E[(\frac{\sqrt{N_x\, N_y\, N_z}}{XYZ} A^T \underline{\hat{F}}_{obs} - \frac{\sqrt{N_x\, N_y\, N_z}}{XYZ} A^T \underline{\hat{F}}_{cal}) \\
&\quad (\frac{\sqrt{N_x\, N_y\, N_z}}{XYZ} A^T \underline{\hat{F}}_{obs} - \frac{\sqrt{N_x\, N_y\, N_z}}{XYZ} A^T \underline{\hat{F}}_{cal})^T] \\
&= \frac{N_x\, N_y\, N_z}{(XYZ)^2} A^T E[(\underline{\hat{F}}_{obs} - \underline{\hat{F}}_{cal})(\underline{\hat{F}}_{obs} - \underline{\hat{F}}_{cal})^T] A \\
&= \frac{N_x\, N_y\, N_z}{(XYZ)^2} A^T E[\underline{\epsilon}\ \underline{\epsilon}^T] A\ . \qquad (3.30)
\end{aligned}$$

From (3.30), it is obvious that the covariance matrix of $\underline{\hat{\rho}}_{obs}$ depends mainly on the covariance matrix of $\underline{\epsilon}$. As we discussed, $\underline{\epsilon}$ is comprised with i.i.d. Gaussian structure factors and constant zeros. For the reason stated below, it is not desired to have constant zeros in $\underline{\epsilon}$, i.e. the probabilistic distributions of all the entries of $\underline{\epsilon}$ are consistent.

Due to the truncation of structure factors by the limiting sphere, after performing 3D DFT, we have periodic replicas of the spherical spectrum repeated at the reciprocal-space grid points. Fig. 3.1(a) illustrates the resulting spectrum in a period box. The white sphere is the original spectrum filtered through the limiting sphere, and the black parts from different spheres are the periodic replicas within the period box.

For the case of the spherical filter (i.e. the limiting sphere), if the Nyquist's frequency is exactly selected, the black parts from different spheres will be drawn close

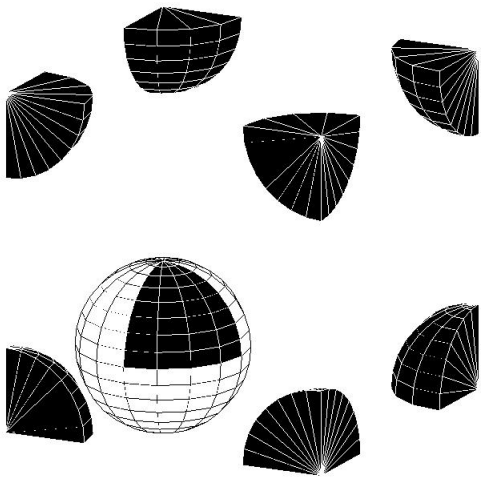

(a) Sphere-case DFT within one period box in reciprocal space

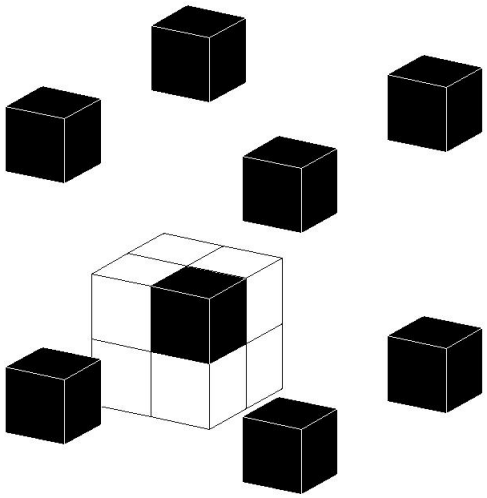

(b) Cube-case DFT within one period box in reciprocal space

Figure 3.1. Comparisons of 3D DFT results between spherical and cubic filters

such that their surfaces just intersect. However, because those parts obey spherical symmetry, there will still be many constant zeros around the center of the given period box. This can be addressed by replacing the spherical filter with a cubic filter. The DFT spectrum pertaining to the cubic filter in the period box is illustrated in Fig. 3.1(b).

It is obvious that by choosing the Nyquist's frequency, the black parts from different cubes will touch the faces of each other, and there will be no constant zeros among the entries of $\underline{\epsilon}$.

To realize the cubic filter, we can eliminate the structure factors near the surface of the limiting sphere, forming a maximum cube enclosed by the limiting sphere. This treatment will definitely degrade the constructed EDM, since we are using fewer structure factors. However, this allows us to analyze the error distribution of electron densities in a simply way, and by selecting the maximum cube, it is also expected the quality of the so-constructed EDM should be fine.

Using the cubic filter and the Nyquist's frequency, $\underline{\epsilon}$ is comprised of pure i.i.d. zero mean, σ_F^2 variance Gaussian random variables, which means $E[\underline{\epsilon}\ \underline{\epsilon}^T] = \sigma_F^2\ I$ (I is an identity matrix). We can rewrite (3.30) as

$$\begin{aligned}
\Sigma &= \frac{N_x\, N_y\, N_z}{(XYZ)^2} A^T \sigma_F^2\ IA \\
&= \frac{N_x\, N_y\, N_z}{(XYZ)^2} \sigma_F^2 A^T A \\
&= \frac{N_x\, N_y\, N_z}{(XYZ)^2} \sigma_F^2 I \\
&= \sigma_\rho^2 I
\end{aligned} \tag{3.31}$$

where $\sigma_\rho^2 = \frac{N_x\, N_y\, N_z}{(XYZ)^2}\sigma_F^2$. (3.31) implies the covariance matrix of the random vector, $\underline{\hat{\rho}}_{obs}$, is constant times an identity matrix; or equivalently, the electron densities of the measured EDM are i.i.d. Gaussian as well. This statistical result comes from the use of the cubic filter and the Nyquist's sampling frequency.

We make a note here, since we cannot measure $\hat{F}_{000_{obs}}$ in an X-ray experiment, the covariance matrix of $\underline{\hat{\rho}}_{obs}$ cannot be perfectly constant times an identity matrix; however, the exact result is $\bar{\Sigma} = \frac{N_x N_y N_z}{(XYZ)^2}\sigma_F^2 \bar{I}$, where the diagonal entries of $\bar{I}$ are $\frac{N_x N_y N_z - 1}{N_x N_y N_z}$'s, and all the other entries are $\frac{-1}{N_x N_y N_z}$'s. As the number of samples is much larger than one, we are confident to make the following approxiamtion $\bar{\Sigma} \approx \frac{N_x N_y N_z}{(XYZ)^2}\sigma_F^2 \, I = \Sigma$.

The reason that it is desired to have the entries of $\underline{\hat{\rho}}_{obs}$ independent or uncorrelated, is illustrated in Fig. 3.2.

In this example, we demonstrate the effect of correlation in a 1D carbon atom's electron densities. We assume the carbon atom is Gaussian-distributed with the standard deviation 0.55Å and 6 electrons spreading around the nuclei. The dimension size of this 1D simulated unit cell is 50Å, and the resolution is 2.5Å, meaning the maximum reciprocal-space index of the measured structure factors is $\frac{50}{2.5} = 20$. For the situation at the Nyquist's sampling frequency, there are $2 \times 20 + 1 = 41$ samples in one unit cell. We generate i.i.d. Gaussian random errors (zero mean and 10^2 variance) among the 40 measured structured factors, and the reconstructed EDM by performing 41-point DFT is shown in Fig. 3.2(a). Since the errors among the reconstructed EDM are uncorrelated and identical, we can easily find out that the scattered points are independent of each other, and bounded by $\pm\sigma_\rho = \pm\frac{\sqrt{N_x}}{X}\sigma_F = \pm\frac{\sqrt{41}}{50}10 = \pm 1.64\mathring{A}^{-1}$ around the true electron density curve. This bound is taken as a *noise bound*, within which the electron densities are totally unreliable. It is also implied that the sub-peaks in the noise bound cannot be counted as possible atomic centers, reducing the risk of overfitting. Furthermore, by taking the noise bound into account, we can fit a modeled electron density function to data very easily since the data is believed to deviate from the modeled function by σ_ρ. For comparison, we also show the over-sampled case as in Fig. 3.2(b) with 1000 samples in the same simulated unit cell. By using the same Gaussian error distribution and adding $1000 - 41 = 959$

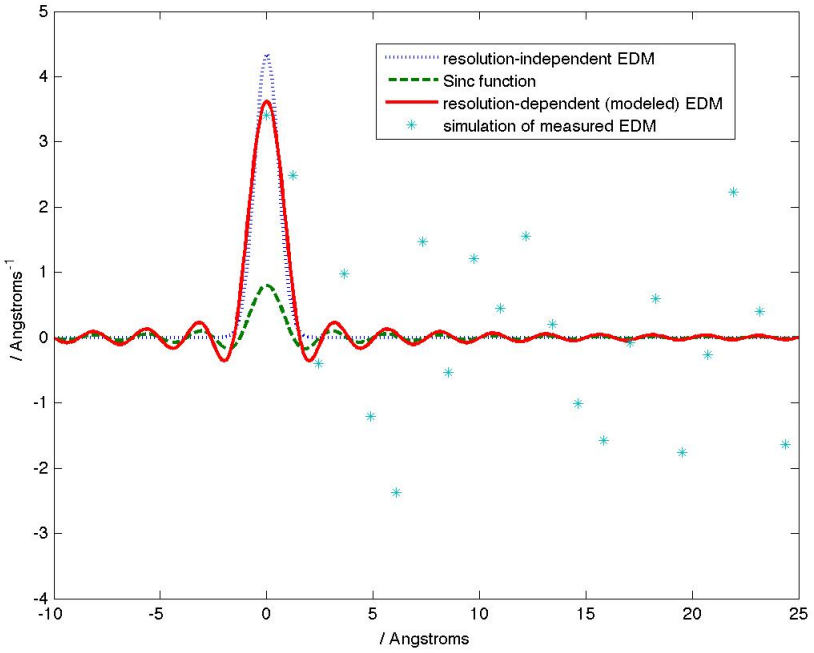

(a) uncorrelated errors at Nyquist's frequency with 41 samples in the unit cell

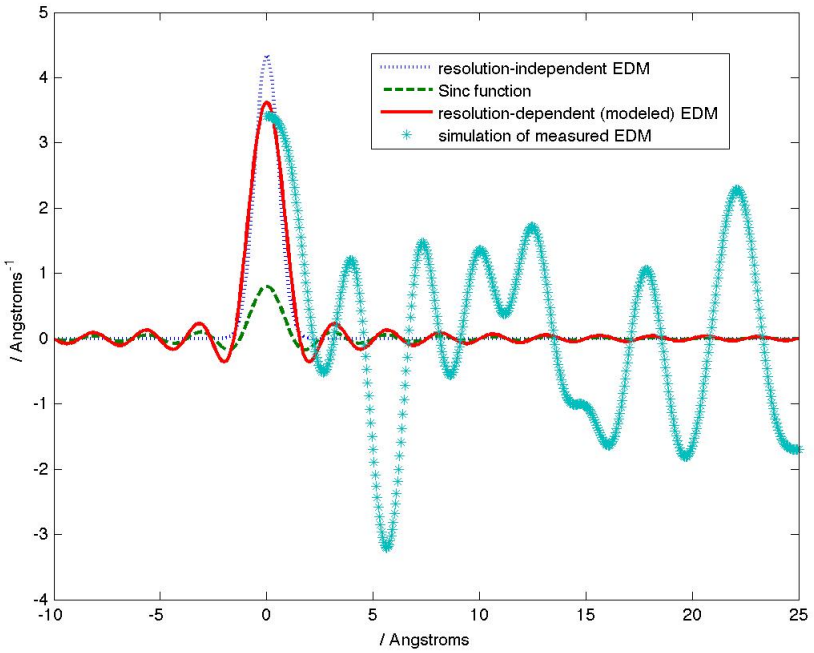

(b) correlated errors with 1000 samples in the unit cell

Figure 3.2. 1D simulation of EDM measurements

constant zeros in the DFT, the errors among the electron density values are strongly correlated. Since the electron density values are not i.i.d. any more in this case, there is no such a uniform noise bound confining the unreliable density values. As a result, fitting a modeled electron density function to the measurements also becomes difficult. Another important application of an uncorrelated EDM is to calculate the confidence probability for decision-makings in real-space refinement (see Section 3.4.2).

3.3 Statistical Properties

As discussed in Section 3.2, if we choose the Nyquist's frequency and the cubic filter, all of the entries in $\underline{\hat{\rho}}_{obs}$ are i.i.d. Gaussian. Note $\underline{\hat{\rho}}_{obs}$ is composed of the real and imaginary parts of all the electron densities in the unit cell. Since the mean value of the electron density is a pure real number, we can only take the real parts in $\underline{\hat{\rho}}_{obs}$. Thus we conclude the so-constructed electron densities (i.e. a subset of entries in $\underline{\hat{\rho}}_{obs}$), are still i.i.d. Gaussian. In other words, the error distribution is equivalent for all the sampled density points in the observed EDM, and the variance is not a function of the position in the unit cell.

3.3.1 Maximum Likelihood (ML) estimate of protein structures

Given a calculated EDM model, the conditional probability distribution function (pdf) of an observed EDM, is

$$\begin{aligned} f(\underline{\hat{\rho}}_{obs} \,|\, \underline{\hat{\rho}}_{cal}) &= \frac{1}{(\sqrt{2\pi})^{N_x N_y N_z} det(\Sigma)} e^{-\frac{1}{2}(\underline{\hat{\rho}}_{obs}-\underline{\hat{\rho}}_{cal})^T \Sigma^{-1} (\underline{\hat{\rho}}_{obs}-\underline{\hat{\rho}}_{cal})} \\ &= \frac{1}{(\sqrt{2\pi}\ \sigma_\rho^2)^{N_x N_y N_z}} e^{-\frac{1}{2}(\underline{\hat{\rho}}_{obs}-\underline{\hat{\rho}}_{cal})^T \Sigma^{-1} (\underline{\hat{\rho}}_{obs}-\underline{\hat{\rho}}_{cal})} \\ &= \frac{1}{(\sqrt{2\pi}\ \sigma_\rho^2)^{N_x N_y N_z}} e^{-\frac{1}{2\sigma_\rho^2}(\underline{\hat{\rho}}_{obs}-\underline{\hat{\rho}}_{cal})^T (\underline{\hat{\rho}}_{obs}-\underline{\hat{\rho}}_{cal})} \end{aligned} \tag{3.32}$$

where $\Sigma^{-1} = \frac{1}{\sigma_\rho^2} \begin{bmatrix} 1 & 0 & \cdots & 0 \\ 0 & 1 & \cdots & 0 \\ \vdots & \vdots & \ddots & \vdots \\ 0 & 0 & \cdots & 1 \end{bmatrix}$.

Let us define Θ as the conformational space. The Maximum Likelihood (ML) estimate of a structural conformation c is formulated as

$$\begin{aligned} c^* &= \arg\max_{c\in\Theta} f(\textit{Local EDM data around } c \mid c) \\ &= \arg\max_{c\in\Theta} f(\underline{\hat{\rho}}_{obs} |\ \underline{\hat{\rho}}_{cal}(c)) \\ &= \arg\max_{c\in\Theta} \frac{1}{(\sqrt{2\pi}\ \sigma_\rho^2)^{N_x N_y N_z}} e^{-\frac{1}{2\sigma_\rho^2}(\underline{\hat{\rho}}_{obs} - \underline{\hat{\rho}}_{cal}(c))^T (\underline{\hat{\rho}}_{obs} - \underline{\hat{\rho}}_{cal}(c))} \\ &= \arg\min_{c\in\Theta} (\underline{\hat{\rho}}_{obs} - \underline{\hat{\rho}}_{cal}(c))^T (\underline{\hat{\rho}}_{obs} - \underline{\hat{\rho}}_{cal}(c)) \\ &= \arg\min_{c\in\Theta} \|\underline{\hat{\rho}}_{obs} - \underline{\hat{\rho}}_{cal}(c)\|^2 \end{aligned} \tag{3.33}$$

where $\underline{\hat{\rho}}_{cal}(c)$ is the resolution-dependent EDM calculated (see Section 2.3) around the local region of the conformation c.

(3.33) implies the ML structural estimate can be expressed as a Least Squares (LS) solution. An application of this ML estimate is to determine the local structure using local EDM, such as side chain assignment, which is discussed in Section 3.4.

3.3.2 Discrete-case Parseval's Theorem

The widely-used description of the real-space fitting error is the mean square error (MSE) of the whole EDM, which is derived from Parseval's Theorem [31]. However, it is a score for the entire EDM, but not for individual sampled density points. Our framework is capable of obtaining the error distribution of the electron density at each sampled point, as shown in Section 3.2. Next, we will show our framework can also handle the Parseval's theorem (i.e. MSE score), which is in a discrete sense.

We use the above formulation to derive the discrete-case Parseval's theorem.

$$\underline{\hat{\rho}}_{obs} = \frac{\sqrt{N_x\, N_y\, N_z}}{XYZ} A^T \underline{\hat{F}}_{obs}$$

$$\underline{\hat{\rho}}_{cal} = \frac{\sqrt{N_x\, N_y\, N_z}}{XYZ} A^T \underline{\hat{F}}_{cal}$$

$$\underline{\hat{\rho}}_{obs} - \underline{\hat{\rho}}_{cal} = \frac{\sqrt{N_x\, N_y\, N_z}}{XYZ} A^T \ (\underline{\hat{F}}_{obs} - \underline{\hat{F}}_{cal})$$

$$(\underline{\hat{\rho}}_{obs} - \underline{\hat{\rho}}_{cal})^T (\underline{\hat{\rho}}_{obs} - \underline{\hat{\rho}}_{cal}) = (\frac{\sqrt{N_x\, N_y\, N_z}}{XYZ})^2 (\ \underline{\hat{F}}_{obs} - \underline{\hat{F}}_{cal})^T\, A\, A^T (\ \underline{\hat{F}}_{obs} - \underline{\hat{F}}_{cal})$$

$$\| \underline{\hat{\rho}}_{obs} - \underline{\hat{\rho}}_{cal} \|^2 = (\frac{\sqrt{N_x\, N_y\, N_z}}{XYZ})^2 \ \| \ \underline{\hat{F}}_{obs} - \underline{\hat{F}}_{cal} \|^2 \tag{3.34}$$

where "$\| \cdot \|$" is the Euclidean norm of a vector. We have used many times the fact that if A is a unitary matrix, $A^T A = A A^T = I$, where I is an identity matrix. Both the observed EDM and the modeled EDM are constructed in the same way to compare with each other. The squared norm of deviation in (3.34) is a widely-used measure of the EDM fitting.

3.4 Decision Making and Confidence Probability

We show the problem of protein side chain assignment (SCA) as an example of performing local real-space refinement. For each amino acid residue, there are finitely many possible side chain conformations, called rotamers. Assuming the backbone and the observed EDM are given, for each residue, a best-fit rotamer can be determined

according to the Maximum Likelihood decision rule. There is definitely uncertainty of making this decision. We define a measure of uncertainty or equivalently, confidence probability, and also propose a numerical way to calculate it.

3.4.1 Decision Rules for Refinement

Let us assume the real-space refinement is performed over a discrete conformation space, e.g. side chain rotamers. It is shown that the ML estimate reduces to a LS solution in Section 3.3.1, which requires to compute the squared Euclidean norm of the density difference vector as a matching score. We postulate that the rotamer with the smallest matching score is the best-fit rotamer.

Decision Rule 1. *For each amino acid residue, there are N possible side chain rotamers. The rotamer set is denoted as $\{r_1, \ldots, r_N\}$. Provided that the backbone is determined, and the local EDM is obtained from an X-ray experiment, the ML estimate of the side chain structure can be selected by the following rule:*

If

$$f(\textit{Local EDM data around } r_k \mid r_k) > f(\textit{Local EDM data around } r_i \mid r_i)$$

for $i = 1, 2, \ldots, N,\ i \neq k$, rotamer r_k is then selected.

From (3.32), the ML estimate is equivalent to the LS solution. Thus, we define the squared norm of the difference, between the observed electron density vector $\underline{\hat{\rho}}_{obs}$ and the calculated vector $\underline{\hat{\rho}}_{cal}(r_k)$, as the matching score, denoted by R_k. Then, we have the following LS decision rule.

Decision Rule 2. *For each rotamer from the rotamer set, a modeled local EDM can be constructed. If the backbone is fixed and the observed EDM is obtained from an*

X-ray experiment, we compute the matching scores for all the N rotamers. The ML estimate of the side chain structure is r_k, if

$$\|\hat{\underline{\rho}}_{obs} - \hat{\underline{\rho}}_{cal}(r_k)\|^2 < \|\hat{\underline{\rho}}_{obs} - \hat{\underline{\rho}}_{cal}(r_i)\|^2 \quad for\ i = 1, 2, \ldots, N,\ i \neq k,$$
$$or \qquad R_k < R_i \quad for\ i = 1, 2, \ldots, N,\ i \neq k. \tag{3.35}$$

3.4.2 Confidence Probability Calculation

According to the LS decision rule, the rotamer with the smallest matching score is always preferable, called the best-fit rotamer. So the confidence probability of the decision-making relies on the statistics of these matching scores. We first study the probability distribution of the matching scores, and then develop a numerical way to calculate the confidence probability.

Let us take a look at the general distribution of the matching scores. For a rotamer r_i of a particular residue, suppose the local EDM around the side chain structure has M sampled density points. The observed electron density vector $\hat{\underline{\rho}}_{obs}$ is the calculated electron density vector of the native side chain conformation plus i.i.d. zero-mean, σ_ρ^2-variance Gaussian errors. Vector $\hat{\underline{\rho}}_{cal}(r_i)$ is calculated using r_i as a structural model of the side chain.

$$\hat{\underline{\rho}}_{obs} = \hat{\underline{\rho}}_{cal}(Native) + \underline{\epsilon_\rho}$$

So the difference vector is given by

$$\hat{\underline{\rho}}_{obs} - \hat{\underline{\rho}}_{cal}(r_i) = [\hat{\underline{\rho}}_{cal}(Native) - \hat{\underline{\rho}}_{cal}(r_i)] + \underline{\epsilon_\rho}\ ,$$

and the matching score is thus the squared Euclidean norm of this difference vector, which is

$$R_i = \|\underline{\hat{\rho}}_{obs} - \underline{\hat{\rho}}_{cal}(r_i)\|^2 \ . \tag{3.36}$$

In another word, R_i is just a sum of M squared Gaussian random variables. Precisely, R_i is a sum of M χ^2 random variables. In practice, we have M greater than 100, so by *Central Limit Theorem*, the summation of χ^2 random variables can be approximated as a single Gaussian random variable. It can be shown that, by utilizing the moments of Gaussian random variables, the mean and the variance of R_i are listed as

$$\begin{aligned} E[R_i] &= \|\underline{\hat{\rho}}_{cal}(Native) - \underline{\hat{\rho}}_{cal}(r_i)\|^2 + M\sigma_\rho^2 \\ Var[R_i] &= 4\sigma_\rho^2\|\underline{\hat{\rho}}_{cal}(Native) - \underline{\hat{\rho}}_{cal}(r_i)\|^2 + 5M\sigma_\rho^4 \ , \end{aligned} \tag{3.37}$$

where $\|\underline{\hat{\rho}}_{cal}(Native) - \underline{\hat{\rho}}_{cal}(r_i)\|^2$ comes from the coordinate errors of the structural model r_i, and σ_ρ^2 is the 2D Gaussian random error due to the missing atoms in the model.

Next, we compute the confidence probability that, the best-fit rotamer returned by the decision rule is coincidentally the *best* rotamer, which is defined as the closest rotamer (i.e. minimum all-atom deviation) to the native side chain structure. Note it is not always the best. Suppose the kth rotamer r_k is the closest rotamer to the native conformation. If we desire to choose this rotamer in the local real-space refinement, according to the LS decision rule, we should have the following condition:

$$R_k < R_i, \quad for\ i = 1, 2, \ldots, N,\ i \neq k. \tag{3.38}$$

So the confidence probability is the probability that (3.38) holds, denoted as $P(R_k < R_i, \quad for\ i = 1, 2, \ldots, N,\ i \neq k)$. Noting all the matching scores are conditionally independent Gaussian random variables with the means and the variances specified in (3.37), the confidence probability can thus be calculated as

$$
\begin{aligned}
& P(R_k < R_i, \quad for\ i = 1, 2, \ldots, N,\ i \neq k) \\
= & \int_{\infty}^{\infty} f(R_k = x) P(R_i > R_k, \quad for\ i = 1, 2, \ldots, N,\ i \neq k | R_k = x)\ dx \\
= & \int_{\infty}^{\infty} f(R_k = x) P(R_i > x, \quad for\ i = 1, 2, \ldots, N,\ i \neq k)\ dx \\
= & \int_{\infty}^{\infty} f(R_k = x) \prod_{\substack{i=1,2,\ldots,N \\ i \neq k}} P(R_i > x)\ dx \\
= & \int_{\infty}^{\infty} f(R_k = x) \prod_{\substack{i=1,2,\ldots,N \\ i \neq k}} [1 - \Phi(R_i < x)]\ dx \\
\approx & \int_{E[R_k]-3\sigma_{R_k}}^{E[R_k]+3\sigma_{R_k}} f(R_k = x) \prod_{\substack{i=1,2,\ldots,N \\ i \neq k}} [1 - \Phi(R_i < x)]\ dx\ . \qquad (3.39)
\end{aligned}
$$

where $\sigma_{R_k} = \sqrt{Var[R_k]}$, and $\Phi(R_i < x)$ is the cumulative distribution function (cdf) of the Gaussian random variable R_i. The last step uses the 3σ *rule* [44] of a Gaussian random variable. For the remaining integral, we can still make use of the *8-division method*, which proves to be an efficient numerical method.

CHAPTER 4

EXPERIMENTAL RESULTS USING X-RAY DATA ONLY

In Section 3.4.1, two decision rules, i.e. ML and LS, are demonstrated. Because of the Gaussian random errors, the two rules are equivalent to each other. We need to validate this probabilistic model for X-ray, and test it over several proteins of varying resolutions.

Specifically, given a candidate rotamer, we use our forward model (2.16) to generate modeled local EDM's. For the current rotamer, the error model in Section 3.3 is then utilized to compute the difference between the model and the observation within the voxel of a single residue. Each rotamer choice thus has a matching score in accordance with the squared Euclidean norm of the difference. The smaller the difference is, the higher matching score.

We run the above algorithm over the following set of proteins at different resolutions. From Table 4.1, it is easy to see that our test set is not biased, since there are lots of residues from both α helices and β sheets. The tendency of the total accuracy from high-quality EDM's to poor-resolution EDM's seems reasonable as well.

For the measure of accuracy, we define the *best* rotamer as the closest rotamer choice to the known structure, which has the minimum all-atom mean square deviation from the known structure as in Section 3.4.2. If the *best-fit* rotamer with the highest matching score is coincidentally the *best* rotamer, we say that this side chain conformation is predicted correctly. Otherwise, the prediction is incorrect.

Fig. 4.1 illustrates the accuracy for each type of amino acid at varying resolutions. Generally speaking, the better the resolution is, the more accurate prediction results.

Note for Arginine (ARG) and Lysine (LYS) have long side chains, which have all of the four χ angles, hence are difficult to predict.

Figure 4.1. Accuracy of the Prediction at Different Resolutions

The accuracy of the residue type MET at 1.5Å is low because the number of samples is small, i.e. there are only five MET residues at 1.5Å resolution in our data set.

The limitation of the decision-making based on X-ray only is the failure of addressing the clashes for long side chain residues (e.g. LYS and ARG). Fig. 5.3 is an illustration of clashes. The best-fit rotamer choice mistakingly orients the long

Test Proteins					
PDB codes	resolution	# of residues	# in α helices	# in β sheets	accuracy
2wfi	0.75Å	179	23	57	98.3%
3iv4	1.5Å	112	55	28	95.9%
2wlw	1.5Å	165	23	57	94.2%
2we2	1.5Å	286	11	124	89.5%
2wiq	2.0Å	259	15	119	89.84%
3fjb	2.0Å	146	9	55	88.43%
2zr4	2.0Å	163	39	36	78.74%
3hb0	2.5Å	274	145	28	86.7%
3imq	2.5Å	141	102	0	79.5%
3hjt	2.5Å	287	119	44	78.5%

Table 4.1. Resolution, secondary structures and accuracy of the tested proteins

side chain overlapping the neighbor residue. It can also be seen that, the electron densities around the best side chain are harder to be detected than those around the backbone. This shows the prediction of side chain conformation (i.e. SCA problem) is a challenging one and more difficult than the backbone determination.

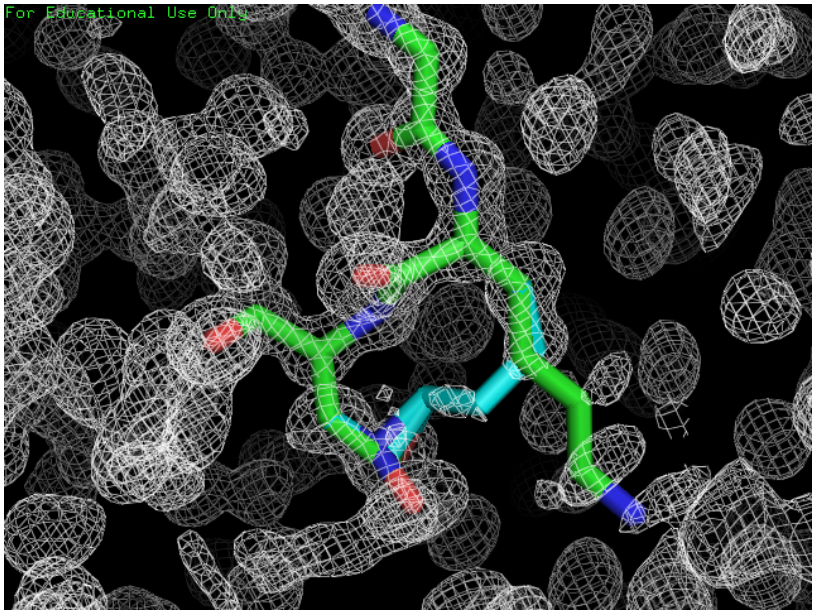

Figure 4.2. The clash occurred in high-quality EDM between LYS and its neighbor residue

The confidence probability calculations are shown in Fig. 4.3. The trend of the confidence probabilities for all types of amino acid is consistent with the accuracy variations. It should be noted that, the values of the confidence probabilities are not exactly correct, since we assume the matching scores are Gaussian variables with the means and variances given in (3.37), which is mainly because the sampled electron density points are Gaussian as well. However, the EDM's we used for these results are from Uppsala Electron Density Server (EDS) [22], which are not constructed using the cubic filter and the Nyquist's frequency (see Chapter 3). The future work is to construct our own EDM's and then perform real-space refinement. Regarding to the use of the confidence probability measure, we propose to run this algorithm for the solved high-quality structures, and then generate another Ramachandran map

for each residue type, which stores the information of the confidence probability. We expect the confidence probability to vary with the amino acid type and the backbone dihedral angles (ϕ, ψ). This Ramachandran map tells us how reliable the side chain conformation can be resolved using X-ray data only. By referring to the map, we suggest crystallographers interpret the unreliable X-ray data meticulously and combine additional sources of data (see Chapter 5).

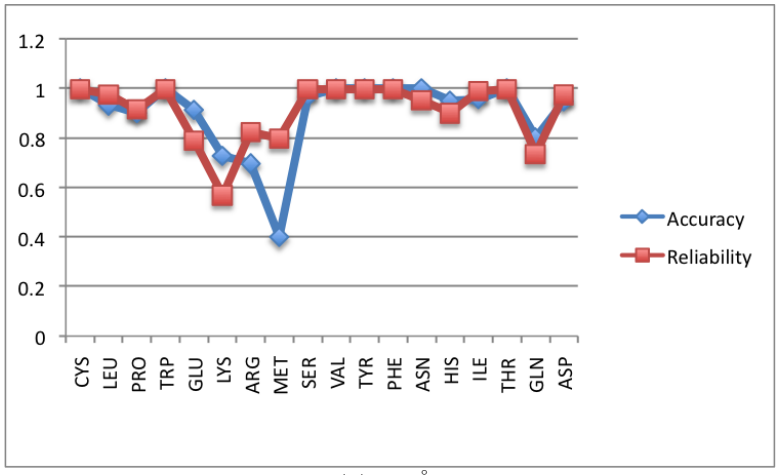

(a) 1.5Å

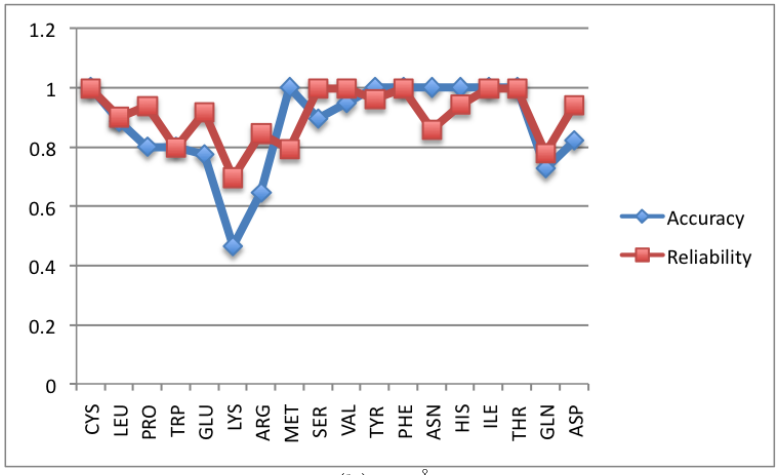

(b) 2.0Å

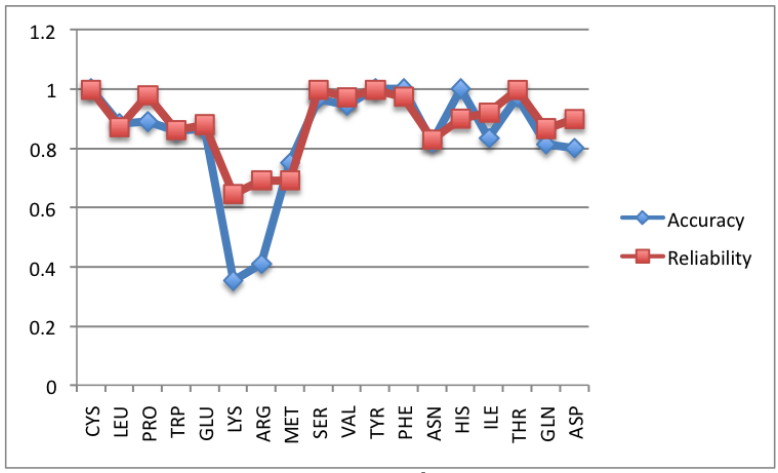

(c) 2.5Å

Figure 4.3. Accuracy vs. Confidence Probability at Different Resolutions

CHAPTER 5

DATA FUSION FOR PROTEIN SIDE CHAIN ASSIGNMENT

We propose a framework to fuse different sources of data for the protein SCA problem. Two essential types of data sources, i.e. NMR and potential energy, are validated in Section 5.1. A data fusion model based on Bayesian inference is presented in Section 5.2, with illustration of the improved prediction results.

5.1 Validation of Multiple Sources of Information

In Chapter 4, it is shown that, for long side chain residue types (e.g. ARG and LYS), the clashes between nearby residues cannot be resolved. From this perspective, we need to add more pairwise restraints detecting and thus eliminating the clashes. There are two possible data sources, one of which is Nuclear Magnetic Resonance (NMR) and the other is stereochemistry (e.g. potential energy calculation).

5.1.1 Nuclear Magnetic Resonance (NMR)

Nuclear Overhauser Effect Spectroscopy (NOESY), which is a specific NMR experiment, provides us distance restraints between atoms from different residues or within the same residue. Habeck et al. introduced a Bayesian inference method [16], which can be incorporated into our probabilistic framework by considering the pairwise restraints as joint probability terms. Here is an example of how we utilize NMR data to correct the errors, caused by the prediction using X-ray data only.

Example 1. *We select ubiquitin with both X-ray and NMR data available. By running the LS decision-making algorithm using X-ray data only, we have the 51st residue (i.e.*

GLU) in chain A predicted incorrectly with the χ_1 angle rotated $108°$*. By searching for the effective pairwise distance restraints between the 51st residue and the nearby residues, we have the following data script in the NMR Restraint Grid of ubiquitin (see Fig. 5.1). The distance between the C_γ atom of the 51st residue (GLU) and*

```
assi
  (  segid "   A" and resid 51   and name  HG# )
  (  segid "   A" and resid 54   and name  HG# )

     4.870     3.070     1.218
```

Figure 5.1. Data Script of Ubiquitin NMR Restraint Grid

the C_γ atom of the 54th residue (ARG) is 4.870 ± 1.218 *with the minimum Van der waals distance 3.070 [34]. The side chain of the 54th residue (ARG) is correctly predicted. Through calculation, the distance between C_γ's respectively from the best rotamer of GLU and ARG's side chain is 4.944; while the distance between C_γ's from the best-fit rotamer of GLU and ARG's side chain is 5.157. So the incorrectly predicted (i.e. best-fit) rotamer has worse NMR matching score than the best rotamer, although the difference is quite small. This is illustrated in Fig. 5.2, which shows the above distances are actually very close to each other.*

From Example 1, we know the NMR distance restraints can be incorporated as pairwise constraints. However, there are very few effective distance restraints in NMR data. In Example 1, the distance restraint is not very effective, either. So NMR data is quite useful in resolving the large-scale or macromolecular structure, but not sensitive to the side chain conformations. Researchers have to use other sources of data, e.g. the geometrical restraints or the physical laws, to correct the prediction errors caused by the X-ray data, e.g. to fully and confidently eliminate the clashes.

5.1.2 Potential Energy Calculation

In physics, it is believed that the natural stable structure should minimize the total potential energy. As a result, the clashes can be avoided by searching for the global energy minimum. For protein structures, there are several types of potential

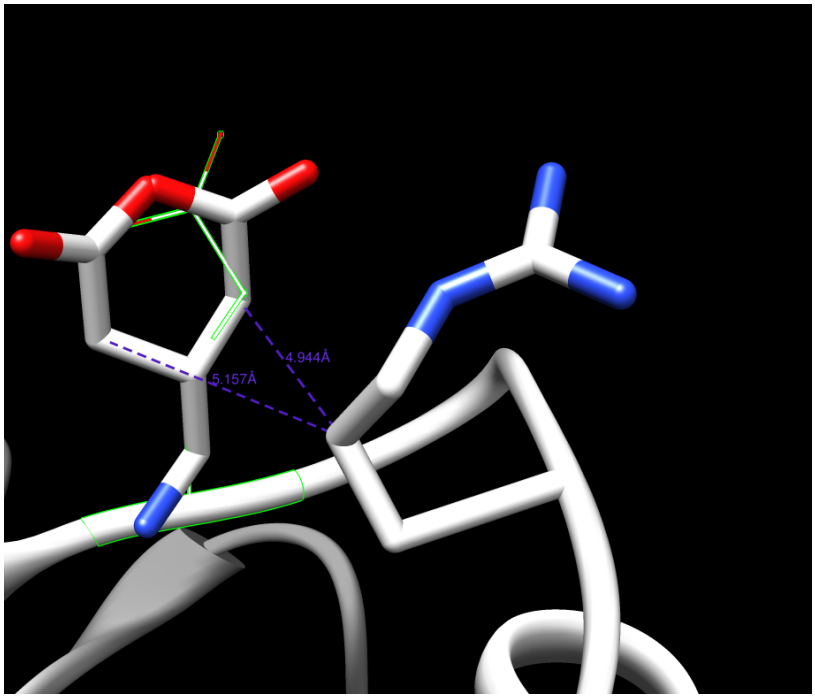

Figure 5.2. The Best Rotamer vs. the Best-fit Rotamer of GLU with the distance between GLU's $C\gamma$ and the nearby ARG's $C\gamma$

energy function, e.g. Amber, CHARMM, etc. The widely used Amber potential is given by [43]

$$V(r^N) = \sum_{bonds} \frac{1}{2} k_b (l - l_0)^2 + \sum_{angles} \frac{1}{2} k_a (\theta - \theta_0)^2 + \sum_{torsions} \frac{1}{2} V_n [1 + \cos(n\omega - \gamma)] + \sum_{j=1}^{N-1} \sum_{i=j+1}^{N} \left\{ \epsilon_{i,j} \left[\left(\frac{\sigma_{ij}}{r_{ij}} \right)^{12} - 2 \left(\frac{\sigma_{ij}}{r_{ij}} \right)^{6} \right] + \frac{q_i q_j}{4\pi\epsilon_0 r_{ij}} \right\} \quad (5.1)$$

The fourth additional term is Van der Waals potential energy function. For simplicity, we only use this potential energy component to indicate the distances between different atomic groups. Since, in physics, potential energy is calculated based on pairwise interactions among the charges, for describing the potential energy of the entire protein, we can group those pairwise interactions into self-energy terms within individual amino acids and pairwise-energy terms between different amino acids. These energy terms are then converted to the *prior* probabilities using Boltzmann distribution [41].

Boltzmann distribution says that, if there are k conformational states in the conformation space Θ, the probability of the kth state is in the negative exponential form with respect to the relative potential energy of that state.

$$P(state_k) = \frac{e^{-(E_k - E_{min})/RT}}{\sum_{k=1}^{N} e^{-(E_k - E_{min})/RT}} \tag{5.2}$$

where $R = 8.31\, J/(mol \cdot K)$ is the molar ideal gas constant and T is the temperature in kelvins (K). The denominator serves as a normalization factor, called the partition function. The smaller the relative potential is, the higher probability the state is observed.

Example 2. *We select the 82nd residue (LYS) from our test protein with pdb code "2zr4". By running the LS decision-making algorithm using X-ray data only, we have a wrong prediction, and the best rotamer ranks the fourth in the descending best-fit rotamer list. The top three best-fit rotamers are illustrated in Fig. 5.3. In Fig. 5.3, the HIS residue is shown to the left, while the LYS residue is displayed to the right and outlined by the green lines. The yellow lines indicate where the clashes occur and the associated potential energies are extremely large.*

For comparison, the best rotamer is shown in Fig. 5.4.

It is obvious that the clashes occur for the top three best-fit rotamer choices, and all of them conflict with the same HIS residue (id:64). By calculating the pairwise-energies between the LYS rotamers and the HIS side chain, the energy values are 22867863.901, $5.27423866577 \times 10^{12}$, 544270475.454 *and* -1.84317088814 *respectively with unit* KJ/mol*, which demonstrates the energy for the best rotamer is extremely smaller than the energies for the clashing best-fit rotamers. This example validates the incorporation of the potential energy as a useful data source to eliminate the clashes.*

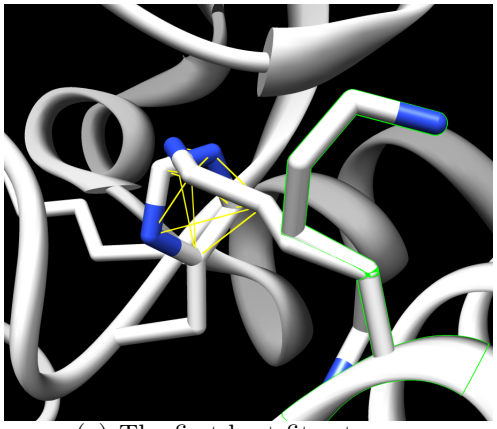

(a) The first best-fit rotamer

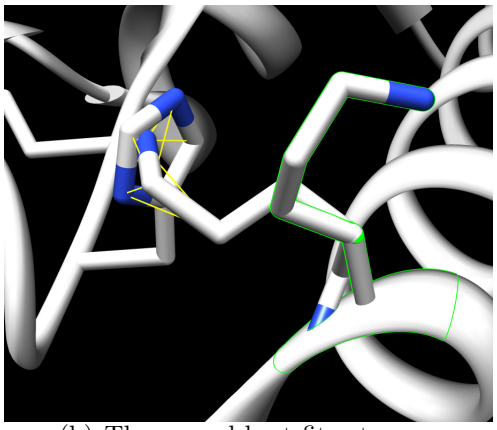

(b) The second best-fit rotamer

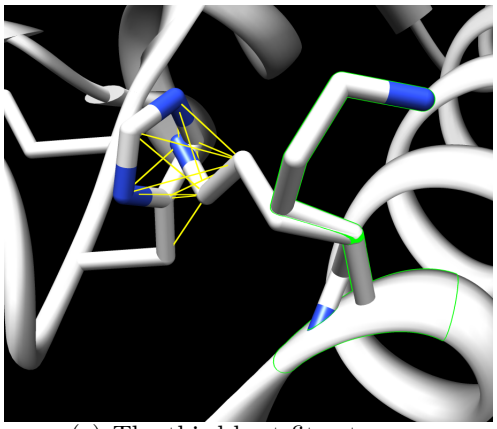

(c) The third best-fit rotamer

Figure 5.3. The top three best-fit rotamers of LYS residue (id: 82) in pdb file "2zr4"

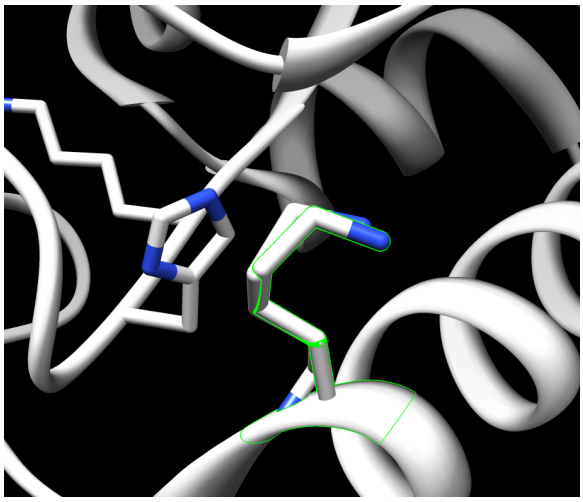

Figure 5.4. The fourth best-fit (also the best) rotamer of LYS residue (id: 82) in pdb file "2zr4"

The question is how to fuse all three sources of data in a reasonable way. By combining the X-ray and NMR data in the form of likelihood, and the potential energy as a prior, it is easy to formulate the *Maximum a posteriori* (MAP) estimation.

5.2 Data Fusion Schemes

The goal of our work is to combine different sources of experimental data and modeling data to firstly solve the SCA problem and then the entire protein structure. Usually, there are two schemes for data fusion. One is named the *pre-detection* fusion, as shown in Fig. 5.5(a). The likelihood functions of multi-sources of data are combined together as a weighted joint likelihood. The weights are assigned according to the reliability of each data source. The other scheme (i.e. *decision* fusion) is suited to the case where the sensors are separately distributed and far away from the fusion center. If the channels, used to transmit detail measurements, are restrained meaning there is information loss, we have to make decisions at the local sensors. The separate decisions are then transmitted to the final fusion center to obtain the final decision, as illustrated in Fig. 5.5(b). Since the latter scheme does not fully take advantage of

the information from the measurements, and our problem is irrelevant to the channel limitation, we propose to use the former scheme.

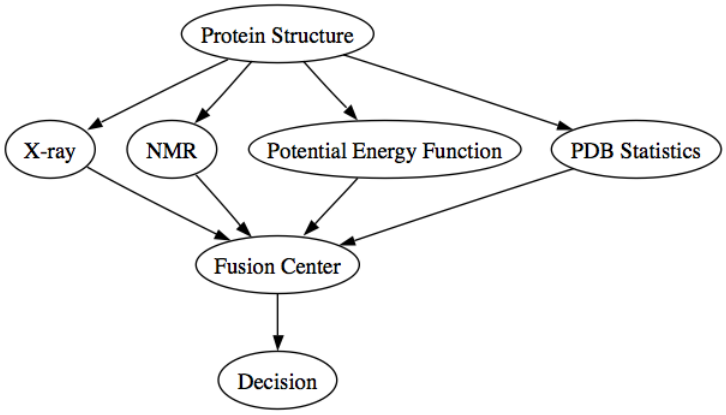

(a) Pre-detection Fusion

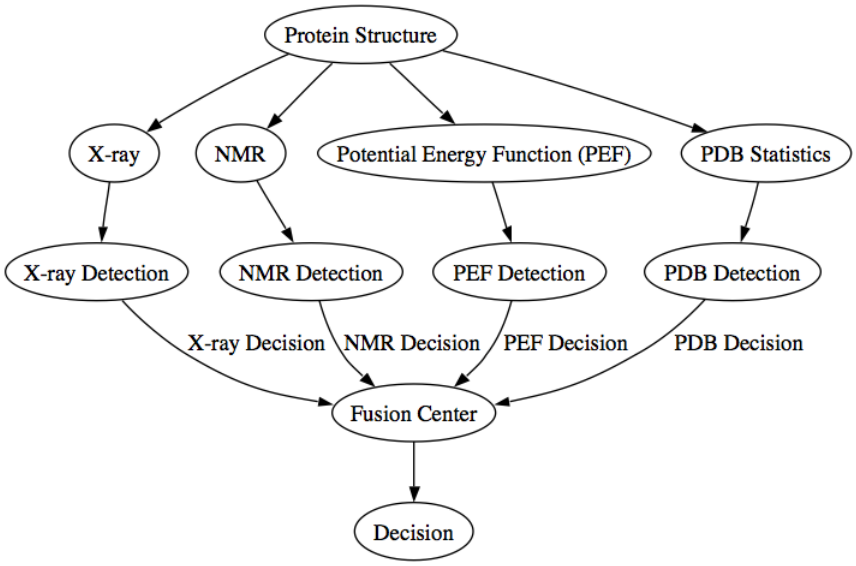

(b) Decision Fusion

Figure 5.5. Data Fusion Schemes

5.2.1 Weighted Bayesian Data Fusion

Bayesian theory is a useful framework to combine different sources of data in a probabilistic way. It derives from a simple relationship between likelihood, priors and posteriors.

Now we extend the problem definition in Section 1.3

$$P(\underline{S}|\, EDM,\, NMR) = \frac{f(EDM,\, NMR\,|\,\underline{S})\, P(\underline{S})}{f(EDM,\, NMR)} \tag{5.3}$$

where the denominator is the partition function acting as a normalization factor, and given by

$$f(EDM,\, NMR) = \sum_{\underline{S}\in\Theta} f(EDM,\, NMR\,|\,\underline{S})\, P(\underline{S}) \tag{5.4}$$

For the prior probability, we use the Boltzmann distribution in (5.2), considering each element $\underline{S} \in \Theta$ to be a conformational state.

$$P(\underline{S}) = \frac{e^{-(E(\underline{S})-E_{min})/RT}}{\sum_{\underline{S}\in\Theta} e^{-(E(\underline{S})-E_{min})/RT}} \tag{5.5}$$

where the potential energy of the protein is composed of self- and pairwise- energy terms, as

$$E(\underline{S}) = \sum_{S_i\in\underline{S}} E_{self}(S_i) + \sum_{\substack{S_i\in\underline{S}\\ S_j\in\underline{S}}} E_{pairwise}(S_i, S_j)\ , \tag{5.6}$$

and $S_i,\ S_j$ are defined in Section 1.3.

So (5.5) can be overwritten as

$$P(\underline{S}) = \prod_{S_i\in\underline{S}} P_{self}(S_i) \prod_{\substack{S_i\in\underline{S}\\ S_j\in\underline{S}}} P_{paiwise}(S_i, S_j)\ . \tag{5.7}$$

Given the structural conformation $\underline{S}$, since different sources of data are class-conditionally independent [38], the joint likelihood function can be factorized in the following way:

$$f(EDM,\, NMR \,|\, \underline{S}) = f(EDM \,|\, \underline{S}) f(NMR \,|\, \underline{S}) \;. \tag{5.8}$$

Regarding the likelihood of X-ray, from Section 3.3, we have already established a way to guarantee all the sampled electron density values are jointly independent given the structure $\underline{S}$.

$$\begin{aligned}
f(EDM \,|\, \underline{S}) &= f(EDM\, around\, \underline{S} \,|\, \underline{S}) \\
&= f(\hat{\underline{\rho}}_{obs} |\; \hat{\underline{\rho}}_{cal}(\underline{S})) \\
&= \frac{1}{(\sqrt{2\pi}\ \sigma_\rho^2)^{N_x N_y N_z}} e^{-\frac{1}{2\sigma_\rho^2} \| \hat{\underline{\rho}}_{obs} - \hat{\underline{\rho}}_{cal}(\underline{S})) \|^2} \\
&= \frac{1}{(\sqrt{2\pi}\ \sigma_\rho^2)^{N_x N_y N_z}} \prod_{S_i \in \underline{S}} e^{-\frac{1}{2\sigma_\rho^2} \| \hat{\underline{\rho}}_{obs} - \hat{\underline{\rho}}_{cal}(\underline{S})) \|^2_{S_i}} \\
&= \prod_{S_i \in \underline{S}} f(Local\, EDM\, around\, S_i \,|\, \underline{S}) \\
&= \frac{1}{(\sqrt{2\pi}\ \sigma_\rho^2)^{N_x N_y N_z}} \prod_{S_i \in \underline{S}} e^{-\frac{1}{2\sigma_\rho^2} \| \hat{\underline{\rho}}_{obs} - \hat{\underline{\rho}}_{cal}(S_i)) \|^2_{S_i}} \\
&= \prod_{S_i \in \underline{S}} f(Local\, EDM\, around\, S_i \,|\, S_i)
\end{aligned} \tag{5.9}$$

where $\| \cdot \|^2_{S_i}$ is the Euclidean norm of the local EDM in the neighborhood of the side chain conformation S_i.

The reason that $f(EDM \,|\, \underline{S})$ can be factorized into $f(Local\, EDM\, around\, S_i \,|\, \underline{S})$'s is because the local EDM's are conditionally i.i.d. Gaussian (see Section 3.2) given the structure.

For good and moderate resolutions (< 2.5Å), we can further factorize $f(Local\ EDM\ around\ S_i \mid \underline{S})$'s into $f(Local\, EDM\, around\, S_i \,|\, S_i)$'s, as shown in the last step. However, this factorization can be more difficult for poor resolutions, since

in that case, the local EDM around S_i is not only determined by itself, but by all the neighbor residues as well.

We can also extend our fusion framework to include NMR data. The interpretation of NMR data is studied by Habeck et al. [16] using a MAP model, so we only give the general fusion expression. For the likelihood of NMR, it is desirable to make all the NMR distance restraints uncorrelated. By applying the similar steps as in (5.9), the decorrelation of NMR data is as

$$\begin{aligned} & f(NMR \,|\, \underline{S}) \\ = \;& f(pairwise\ NMR\ distance\ restraints \mid \underline{S}) \\ = \;& \prod_{\substack{S_i \in \underline{S} \\ S_j \in \underline{S}}} f(distance\ restraints\ between\ S_i\ and\ S_j \mid \underline{S}) \\ = \;& \prod_{\substack{S_i \in \underline{S} \\ S_j \in \underline{S}}} f(distance\ restraints\ between\ S_i\ and\ S_j \mid S_i,\ S_j)\ . \end{aligned} \tag{5.10}$$

Thus the *Maximum a posteriori (MAP)* estimate is given by

$$\begin{aligned} \underline{S}^* &= \arg\max_{\underline{S} \in \Theta} f(EDM, NMR \mid \underline{S})\ P(\underline{S}) \\ &= \arg\max_{\underline{S} \in \Theta} f(EDM \mid \underline{S})\ f(NMR \mid \underline{S})\ P(\underline{S}) \\ &= \arg\max_{\underline{S} \in \Theta} \prod_{S_i \in \underline{S}} f(Local\ EDM\ around\ S_i \mid S_i) \\ &\quad \prod_{\substack{S_i \in \underline{S} \\ S_j \in \underline{S}}} f(distance\ restraints\ between\ S_i\ and\ S_j \mid S_i,\ S_j) \\ &\quad \prod_{S_i \in \underline{S}} P_{self}(S_i) \prod_{\substack{S_i \in \underline{S} \\ S_j \in \underline{S}}} P_{paiwise}(S_i,\ S_j) \\ &= \arg\max_{\underline{S} \in \Theta} \prod_{S_i \in \underline{S}} f_{X-ray}(S_i) P_{self}(S_i) \\ &\quad \prod_{\substack{S_i \in \underline{S} \\ S_j \in \underline{S}}} f_{NOESY}(S_i,\ S_j) P_{paiwise}(S_i,\ S_j)\ . \end{aligned} \tag{5.11}$$

In practice, the above Bayesian framework is widely used with minor modifications, due to the different reliabilities of various data sources. Swain [38] shows the data fusion of multiple sources of remote sensing data, and for the first time assigns the reliability weights to these probabilities and pdf's. Reliability is denoted by a real number α, where $\alpha \in [0, 1]$. The meaning of this measure is by how much percent, we would like to rely on this data source. Usually, by involving the reliability measures, various types of data can be put on a comparable scale.

So the MAP estimate is overwritten as

$$\begin{aligned} \underline{S}^* &= \arg\max_{\underline{S}\in\Theta} \prod_{S_i\in\underline{S}} f_{Xray}(S_i)^{\alpha_{Xray}} P_{self}(S_i)^{\alpha_E} \\ &\quad \prod_{\substack{S_i\in\underline{S} \\ S_j\in\underline{S}}} f_{NOESY}(S_i,\ S_j)^{\alpha_{NOESY}} P_{paiwise}(S_i,\ S_j)^{\alpha_E} \ . \end{aligned} \tag{5.12}$$

It is apparent that the X-ray measurements provide more *experimental self-energy* terms and the merit of NMR NOESY data is to supplement *experimental pairwise-energy* terms. If we take the minus logarithm of the posterior probability, we end up with a modified potential energy, which is derived in a wealth of references [2]. The X-ray matching score is considered as a pseudo-energy term, which is included by the potential energy in terms of linear combination.

5.2.2 Results of Data Fusion for a Simplified SCA Problem

A data fusion scheme based on Bayesian inference is given in Section 5.2.1. We then verify the above idea for a simplified problem, which is not to determine the conformation for all the residues, but only the LYS residues. The LYS residues, that are not correctly predicted in Chapter 4 using X-ray data only, were chosen. Although the problem is hereby simplified, it can still demonstrate a picture of how the data fusion improves the prediction results, and what the reliability measures of different data sources should be like. For the reasons above, we assume all the side chains are

correct except those LYS's, and the reliability of NMR NOESY, α_{NOESY}, is set to 0, since there is few effective NMR data.

The MAP estimate for this simplified problem is then

$$\begin{aligned} S_i^* &= \arg\max_{S_i \in \Theta_i} f_{Xray}(S_i)^{\alpha_{Xray}} \\ &\quad [P_{self}(S_i) \prod_{S_j \neq S_i} P_{paiwise}(S_i,\ S_j)]^{\alpha_E} \end{aligned} \tag{5.13}$$

where Θ_i is the conformation space for the current LYS residue.

In this problem, if the reliabilities are ignored, the prediction is strongly biased to some rotamer choice either with the lowest X-ray matching score or the lowest potential energy. For the likelihood of X-ray, the reliability is low, because the sampled electron density points are not i.i.d. Gaussian. For the priors, converted by the Boltzmann distribution, the variance of the potential energies is much larger than expected, as seen in Example 2. Without involving the reliability, moderate high potentials are then mistakingly considered as indicators of the clashes. So it is necessary to introduce reliability measures, and also they are supposed to be very small numbers so that the prediction is not biased toward any particular rotamer choice. We choose $\alpha_{Xray} = 1\%, \alpha_E = 0.002\%$, which provides a balance of detecting the real clashes and keeping the moderate high potential rotamers.

The prediction results for the LYS residues at varying resolutions are illustrated below. As seen in Fig. 5.6, the x-axis represents separate LYS residues, which are not predicted correctly using X-ray data only in Chapter 4, and the y-axis indicates the rank of the best rotamer in the best-fit rotamer list. The smaller the y-axis ranking index is, the higher probability we make a correct prediction by selecting the best-fit rotamer. After incorporating potential energy, the clashes caused by using the X-ray data only, are eliminated. As the resolution becomes poorer, we expect to make more corrections by increasing the rank of the best rotamer in the best-fit rotamer list,

which is clearly shown in Fig. 5.6(a)-(c). It can also be seen in Fig. 5.6, although most of the LYS's cannot be predicted correctly after data fusion, the rank of the best rotamer is indeed improved after data fusion, and the rank enrichments are 0 for 1.5Å, 2 for 2.0Å, and 2.625 for 2.5Å. We conclude that data fusion is essential for protein structure determination at poor resolutions, where X-ray data provides less information.

Using this fusion method, we expect to eliminate all the undesirable clashes, and increase the prediction accuracy, of the worst-case protein (pdb code: 3hjt) in our test set, from 78.5% to 83.2%. For the remaining discrepancy (i.e. from 83.2% to 100%), it seems no more benefits can be extracted from the potential energy. However, improvement can be made in the utilization of the X-ray data, by sampling the conformational space as fine as possible, since the rotamers cannot fully describe the side chain conformations. Also, the EDM should be constructed in the way we introduced in Chapter 3, so that the probability distributions of sampled density points are i.i.d. Gaussian, which makes the X-ray likelihood more precise and informative.

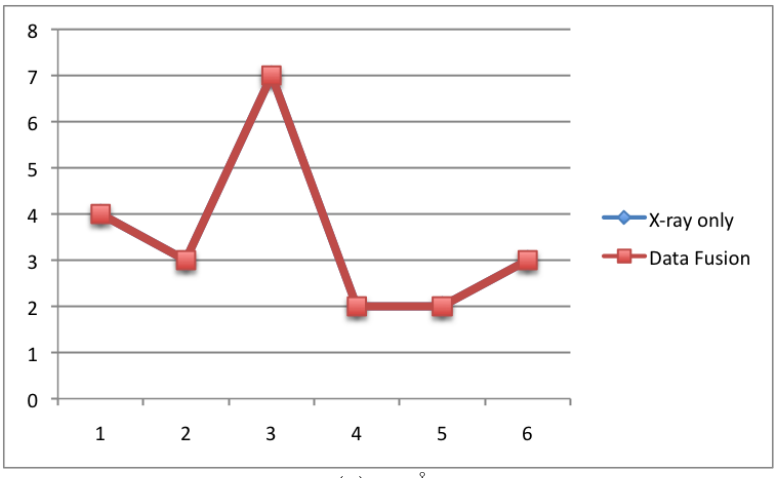

(a) 1.5Å

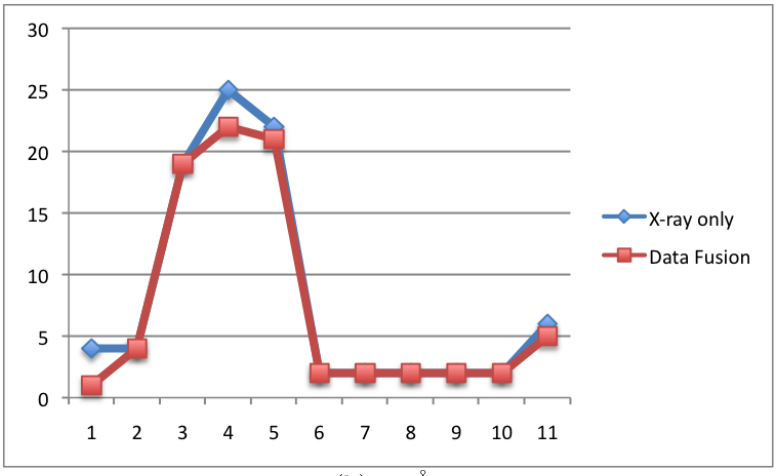

(b) 2.0Å

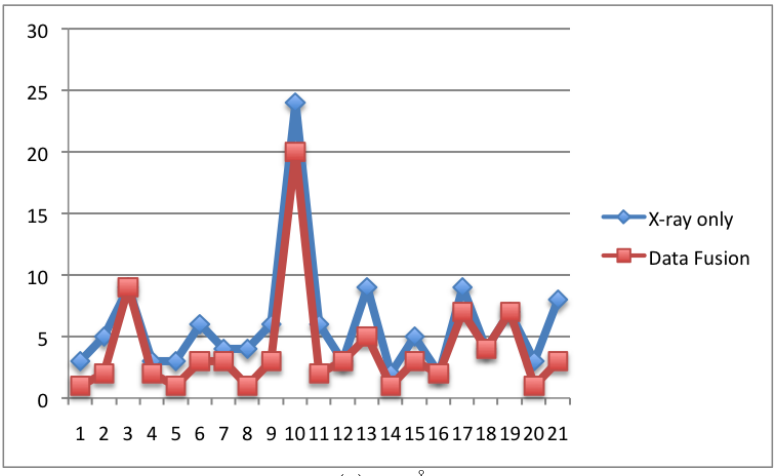

(c) 2.5Å

Figure 5.6. Data fusion vs. X-ray data only for the prediction of LYS residues at different resolutions

CHAPTER 6

CONCLUSIONS AND FUTURE WORK

A novel real-space interpretation method of X-ray crystallography data is introduced. First of all, the widely used Gaussian-distributed atomic model is used as the resolution-independent EDM model. By involving *Signal Processing* theory to describe the X-ray data collection, the resolution-dependent EDM model is obtained through a 3D convolution, which can be computed numerically by the *8-division method*. Besides this *forward model*, the error propagation from structure factor domain to electron density domain is studied, and an *error model* is given. The sampled electron densities and the measured structure factors are related in terms of DFT. The aliasing problem is addressed by choosing the sampling frequency to the Nyquist's frequency. Assuming the structure factors are i.i.d. Gaussian, and noting the DFT is a unitary transformation, the sampled electron densities in the resolution-dependent EDM can be i.i.d. Gaussian as well. To guarantee this, note the limiting cube and the Nyquist's sampling frequency are utilized. For the i.i.d. Gaussian error distribution, the ML estimate is equivalent to the LS solution. According to the LS decision rule, the best-fit rotamer is always chosen for the problem of side chain assignment (SCA), and the confidence probability of the decision-making can be calculated numerically using 8-division method. Results for both the prediction accuracy, and the confidence probability calculations are illustrated.

A data fusion scheme is presented using weighted Bayesian inference. The current framework is capable of fusing the X-ray EDM and the NMR distance restraints as likelihood functions, and the stereochemical (i.e. potential energy) restraints as

priors. To put multiple sources of data on a comparable scale, the reliability weights are assigned to individual data sources, accounting for the percentage of the reliable data from each data source. Improved results are shown for the fusion of the X-ray EDM and the potential energy, which is validated with a simplified problem of LYS side chain assignment. The undesirable structural clashes are successfully eliminated by the incorporation of the stereochemical restraints. The fusion scheme can be easily adapted to many other applications.

For the extension of the work described in this thesis, the likelihood of X-ray data can be improved. The advanced techniques for measuring the phase information, renew the general interest in developing the real-space refinement of X-ray data, which deserves further exploration. As for solving the SCA problem, using the X-ray data interpretation method described in this thesis, the discrete conformational space (i.e. side chain rotamers) should be replaced with the continuous conformation space. Using the modeled data in Chapter 2 and the fitting criterion in Chapter 3, the global minimum of the squared norm (i.e. the LS solution) can be obtained analytically. This requires to compute the derivatives of the squared norm, either with respect to all-atom coordinates [8] [4] [37], or with respect to all the torsion angles [8], in which case the number of parameters to be refined is remarkably reduced.

BIBLIOGRAPHY

[1] Benediktsson, J., Swain, P.H., and Ersoy, O.K. Neural network approaches versus statistical methods in classification of multisource remote sensing data. *IEEE Transactions on Geoscience and Remote Sensing 28*, 4 (1990), 540–552.

[2] Brünger, A.T., Adams, P.D., and Rice, L.M. Recent developments for the efficient crystallographic refinement of macromolecular structures. *Current opinion in structural biology 8*, 5 (1998), 606–611.

[3] Brown, T. L. *Making Truth: The Roles of Metaphor in Science.* University of Illinois Press, 2003.

[4] Chapman, M.S. Restrained real-space macromolecular atomic refinement using a new resolution-dependent electron-density function. *Acta Crystallographica Section A: Foundations of Crystallography 51*, 1 (1995), 69–80.

[5] Chen, B., and Varshney, P.K. A Bayesian sampling approach to decision fusion using hierarchicalmodels. *IEEE Transactions on signal processing 50*, 8 (2002), 1809–1818.

[6] Chesick, J.P. Fourier analysis and structure determination. Part III. X-ray crystal structure analysis. *Journal of Chemical Education 66*, 5 (1989), 413.

[7] Cowtan, K. Fast Fourier feature recognition. *Acta Crystallographica Section D: Biological Crystallography 57*, 10 (2001), 1435–1444.

[8] Diamond, R. A real-space refinement procedure for proteins. *Acta Crystallographica Section A: Crystal Physics, Diffraction, Theoretical and General Crystallography 27*, 5 (1971), 436–452.

[9] DiMaio, F., Shavlik, J., and Phillips, G.N. A probabilistic approach to protein backbone tracing in electron density maps. *Bioinformatics 22*, 14 (2006), e81.

[10] Drenth, J. *Principles of protein X-ray crystallography.* Springer Verlag, 1999.

[11] Dunbrack, R.L., et al. Backbone-dependent rotamer library for proteins application to side-chain prediction. *Journal of Molecular Biology 230*, 2 (1993), 543–574.

[12] Dunbrack, R.L., et al. Rotamer libraries in the 21st century. *Current opinion in structural biology 12*, 4 (2002), 431–440.

[13] Emsley, P., Lohkamp, B., Scott, WG, and Cowtan, K. Features and development of Coot. *Acta Crystallographica Section D: Biological Crystallography 66*, 4 (2010), 486–501.

[14] Fong, Rosamaria. Introductory applied chemistry. `nobel.scas.bcit.ca/.../unit4/4.8_atomicSize.htm`, Feburary 2010.

[15] Fujinaga, M., Gros, P., and Van Gunsteren, WF. Testing the method of crystallographic refinement using molecular dynamics. *Journal of Applied Crystallography 22*, 1 (1989), 1–8.

[16] Habeck, M., Nilges, M., and Rieping, W. Bayesian inference applied to macromolecular structure determination. *Physical Review E 72*, 3 (2005), 31912.

[17] Holton, T., Ioerger, T.R., Christopher, J.A., and Sacchettini, J.C. Determining protein structure from electron-density maps using pattern matching. *Acta Crystallographica Section D: Biological Crystallography 56*, 6 (2000), 722–734.

[18] Jann, Rebecca C. The secret of life. `campus.queens.edu/.../bio103/labs/L6video.htm`, September 2002.

[19] Jeon, B., and Landgrebe, D.A. Decision fusion approach for multitemporal classification. *IEEE Transactions on Geoscience and Remote Sensing 37*, 3 (1999), 1227–1233.

[20] Jones, T.A., Zou, J.Y., Cowan, SW, and Kjeldgaard, M. Improved methods for building protein models in electron density maps and the location of errors in these models. *Acta Crystallographica Section A: Foundations of Crystallography 47*, 2 (1991), 110–119.

[21] Kavraki., Lydia E. Representing proteins in silico and protein forward kinematics. `http://cnx.org/content/m11621/latest/`, June 2007.

[22] Kleywegt, G.J., Harris, M.R., Zou, J., Taylor, T.C., Wahlby, A., and Jones, T.A. The Uppsala electron-density server. *Acta Crystallographica Section D: Biological Crystallography 60*, 12 (2004), 2240–2249.

[23] Klug, A. Joint probability distribution of structure factors and the phase problem. *Acta Crystallographica 11*, 8 (1958), 515–543.

[24] Lovell, S.C., Word, J.M., Richardson, J.S., and Richardson, D.C. The penultimate rotamer library. *Proteins: Structure, Function, and Bioinformatics 40*, 3 (2000), 389–408.

[25] Lucibella, Mike, and Schenkman, Lauren. First detailed photos of atoms. `http://www.insidescience.org/research/first_detailed_photos_of_atoms`, September 2009.

[26] Morris, R.J., Perrakis, A., and Lamzin, V.S. ARP/wARP's model-building algorithms. I. The main chain. *Acta Crystallographica Section D: Biological Crystallography 58*, 6 (2002), 968–975.

[27] Morris, R.J., Zwart, P.H., Cohen, S., Fernandez, F.J., Kakaris, M., Kirillova, O., Vonrhein, C., Perrakis, A., and Lamzin, V.S. Breaking good resolutions with ARP/wARP. *Journal of synchrotron radiation 11*, 1 (2003), 56–59.

[28] Navaza, J. On the computation of structure factors by FFT techniques. *Acta Crystallographica Section A: Foundations of Crystallography 58*, 6 (2002), 568–573.

[29] Patterson, AL. The diffraction of X-rays by small crystalline particles. *Physical Review 56*, 10 (1939), 972–977.

[30] Read, RJ. Structure-factor probabilities for related structures. *Acta Crystallographica Section A: Foundations of Crystallography 46*, 11 (1990), 900–912.

[31] Read, R.J. Protein crystallography course. `http://www-structmed.cimr.cam.ac.uk/course.html`, November 2005.

[32] Rossmann, MG, and Blow, D.M. The detection of sub-units within the crystallographic asymmetric unit. *Acta Crystallographica 15*, 1 (1962), 24–31.

[33] Rupp, Bernhard. Introduction to data collection. `www.ruppweb.org/Xray/tutorial/datacoll.htm`, December 2009.

[34] Sapay, N. noe2xplor.py. `http://pbil.ibcp.fr/~nsapay/downloads/README_noe2xplor.txt`, September 2004.

[35] Sayre, D. The calculation of structure factors by Fourier summation. *Acta Crystallographica 4*, 4 (1951), 362–367.

[36] Sidhu, Hardeep. Amino acid helps protein grow tooth enamel. `http://www.topnews.in/amino-acid-helps-protein-grow-tooth-enamel-2246434`, December 2009.

[37] Sussman, J.L., Holbrook, S.R., Church, G.M., and Kim, S.H. A structure-factor least-squares refinement procedure for macromolecular structures using constrained and restrained parameters. *Acta Crystallographica Section A: Crystal Physics, Diffraction, Theoretical and General Crystallography 33*, 5 (1977), 800–804.

[38] Swain, P.H., Richards, J.A., and Lee, T. Multisource data analysis in remote sensing and geographic information processing. In *Proc. 11th Int. Symp. Machine Processing of Remotely Sensed Data 1985*, pp. 211–217.

[39] Ten Eyck, L.F. Efficient structure-factor calculation for large molecules by the fast Fourier transform. *Acta Crystallographica Section A: Crystal Physics, Diffraction, Theoretical and General Crystallography 33*, 3 (1977), 486–492.

[40] Terwilliger, T.C. Automated side-chain model building and sequence assignment by template matching. *Acta Crystallographica Section D: Biological Crystallography 59*, 1 (2002), 45–49.

[41] Thornton, J.M., and Bayley, P.M. Conformational energy calculations for dinucleotide molecules. A study of the component mononucleotide adenosine 3'-monophosphate. *Biochemical Journal 149*, 3 (1975), 585.

[42] van Zoelen, E.J. J. Introduction to homology modeling. `http://www.cmbi.ru.nl/~hvensela/EGFR-verslag/`.

[43] Wikimedia Foundation, Inc. Amber. `http://en.wikipedia.org/wiki/AMBER`, April 2010.

[44] Wikimedia Foundation, Inc. Normal distribution. `http://en.wikipedia.org/wiki/Normal_distribution`, August 2010.

[45] Zou, J.Y., and Jones, T.A. Towards the automatic interpretation of macromolecular electron-density maps: qualitative and quantitative matching of protein sequence to map. *Acta Crystallographica Section D: Biological Crystallography 52*, 4 (1996), 833–841.